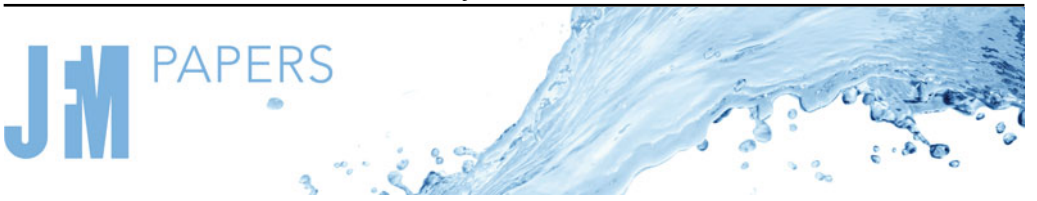
J. Fluid Mech. (2026), *vol.* 1037, A51, doi:10.1017/jfm.2026.11716



Dry and cohesive granular flows in a rotating drum: flow dynamics and scaling behaviours

Zhongrong Wang[1], **Annan Zhou**[1], **Teng Man**[2], **Wantao Ding**[3] and **Herbert Huppert**[4]

[1]Discipline of Civil and Infrastructure Engineering, School of Engineering, Royal Melbourne Institute of Technology (RMIT), Victoria 3001, Australia

[2]College of Civil Engineering, Zhejiang University of Technology, 288 Liuhe Road, Hangzhou, Zhejiang 310023, PR China

[3]School of Qilu Transportation, Shandong University, Jinan 250002, PR China

[4]Institute of Theoretical Geophysics, King's College, University of Cambridge, King's Parade, Cambridge CB2 1ST, UK

Corresponding author: Annan Zhou, annan.zhou@rmit.edu.au

(Received 13 December 2025 UTC; revised 28 March 2026 UTC; accepted 17 May 2026 UTC)

Understanding the rheology of granular surface flows remains a significant challenge, particularly when inertial and cohesive interactions occur between particles to trigger complex regime transitions. This study investigates the steady flow dynamics of dry and cohesive granular materials through systematic rotating drum experiments, focusing on the effects of rotation speed, drum-to-particle size ratio and cohesion level. Scaling laws were further established to capture the combined effects of these factors and provide a unified description of flow behaviour across both dry and cohesive regimes. Results show that, for dry granular flows, both the normalised flowing layer thickness δ_0/d where δ_0 is flowing layer thickness and d represents the particle diameter and dynamic angle of repose tan β_0 increase with Froude number, with a critical transition angle of tan $\beta_0 \approx 0.58$ marking the onset of cascading. The presence of interstitial liquid induces capillary cohesion, leading to a plug-like flow with a convex free surface and higher β_0 and δ_0. A new dimensionless governing parameter, derived from dimensional analysis incorporating a capillary time scale, successfully collapses nearly all experimental data onto single master curves that exhibit clear power-law behaviour, capturing the combined effects of inertia, size and cohesion. Furthermore, rheological interpretation within the $\mu(I)$ framework, where μ represents the effective friction coefficient and I denotes the inertial number reveals rate-

© The Author(s), 2026. Published by Cambridge University Press. This is an Open Access article, distributed under the terms of the Creative Commons Attribution licence (https://creativecommons.org/licenses/by/4.0/), which permits unrestricted re-use, distribution and reproduction, provided the original article is properly cited.

https://doi.org/10.1017/jfm.2026.11716 Published online by Cambridge University Press

dependent frictional strengthening for both dry and cohesive cases, with cohesive flows exhibiting consistently higher resistance induced by interparticle capillary cohesion.

Key words: rotating flows, avalanches, granular media

1. Introduction

Unlike ordinary fluids, a granular packing can remain at rest even with an inclined free surface. This seemingly simple observation points to a key feature of granular matter: the intrinsic dissipative nature of interparticle interactions, which distinguishes granular materials from conventional solids, liquids and gases (Thompson & Huppert 2007; Coppin *et al.* 2023; Wang *et al.* 2026*a*, 2026*b*). When the slope exceeds a critical threshold, a phase transition from a solid-like to a fluid-like state occurs (Bonamy, Daviaud & Laurent 2002; Marteau & Andrade 2018), giving rise to a free-surface flow characterised by a thin granular flowing layer near the unconfined surface and a largely static bulk underneath (Dong *et al.* 2023; Man, Huppert & Galindo-Torres 2025). The highly intricate and heterogeneous nature of such flows makes their dynamics challenging to characterise and predict. As a primary example, landslides exhibit this surface dynamics (Lucas, Mangeney & Ampuero 2014; Bouchut *et al.* 2016; Man *et al.* 2021, 2026); however, recent events have shown that they can initiate on slopes below 5° and propagate over remarkably long distances, far beyond the limits predicted by conventional stability analyses (Gee *et al.* 2007; Dai *et al.* 2025). This highlights the limitations of current understanding of granular surface flows and the need for deeper insight to improve natural hazard assessment and risk mitigation.

Understanding the mechanisms governing granular surface flows often involves specific experimental configurations capable of producing prototypical flows. Among these, the rotating drum has been widely recognised as a benchmark test model due to its relatively simple geometry and rich surface flow dynamics (Chen *et al.* 2024; Maguire *et al.* 2024; Vu *et al.* 2024; Jin *et al.* 2025). In this configuration, a steady flow can be achieved through gravity-driven surface motion as drum rotation continuously transports the granular material upward. The corresponding flow field consists of an upward, solid-like rigid motion following the drum wall, downward surface flow and a well-defined free surface, sharing the same physical characteristics as the typical granular surface flows discussed above (Orpe & Khakhar 2007; Wang *et al.* 2025), as shown in figure 1.

Based on the rotating drum apparatus, which provides a controllable and repeatable environment for systematic investigation, the flow dynamics of granular materials has been extensively studied, with particular attention to their dependence on rotation speed (Rajchenbach 1990), drum size (Orozco *et al.* 2020) and particle properties (Ma & Zhao 2018). In particular, with an increase in rotation speed for a given granular assembly, the flow can be classified into six distinct surface flow regimes (Mellmann 2001; Dong *et al.* 2023), among which the rolling and cascading regimes are the most representative, as they correspond to continuous and steady surface flows with a nearly flat or S-shaped free surface (Govender 2016). In both regimes, the influence of these system parameters on granular flow is commonly characterised by the evolution of the free-surface profile and bulk flow quantities, such as the flowing layer thickness δ_0 and dynamic angle of repose β_0 (Pignatel *et al.* 2012). As such, it has been reported that the normalised flowing layer thickness δ_0/d, where d is the particle diameter, follows a power-law relationship with the rotation speed ω as $\delta_0/d \propto \omega^n$, with the exponent n varying from 0.17 to 0.68 as the drum-to-particle size ratio D/d increases (Félix *et al.* 2007). While not a dimensionally strict scaling law, this relation provides a phenomenological fit that captures the observed experimental trends. In a similar manner, the maximum surface angle has been found to

https://doi.org/10.1017/jfm.2026.11716 Published online by Cambridge University Press

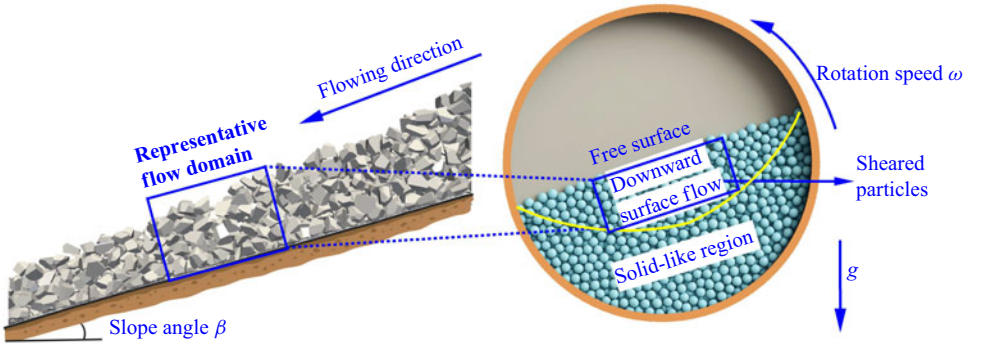


Figure 1. Conceptual illustration of granular surface flow and its analogue in a rotating drum. The yellow solid line marks the interface between the downward surface flow and solid-like region.

increase systematically with both ω and D/d, whereas the latter effect tends to saturate at larger D/d values (Chou & Hsiau 2012; Orozco *et al.* 2020; Preud'homme *et al.* 2021).

However, most previous investigations have been limited to dry granular flows in rotating drums, and the mechanism governing the flow dynamics of cohesive granular materials remains elusive. In fact, granular materials in natural hazards often involve interstitial fluids (Jarray, Magnanimo & Luding 2019; Liu *et al.* 2021; Dai *et al.* 2025). The presence of even a small amount of liquid can significantly alter the dynamic response of granular assemblies, which is attributed to the additional cohesion generated by non-uniform liquid bridges connecting contacting or neighbouring particles (Brewster, Grest & Levine 2009; Liao & Huang 2021). Compared with the cohesionless cases, the work of Tegzes, Vicsek & Schiffer (2003), Alexander *et al.* (2006) and Pol, Artoni & Richard (2025) demonstrated that cohesive granular systems exhibit even more complex flow behaviour, as interparticle cohesion can give rise to new motion regimes and a distinct avalanche dynamics. Specifically, as cohesion increases, the surface flow gradually transitions toward a plug flow, characterised by a plug-like region overlying a lower shear band (Rognon *et al.* 2008; Mandal, Nicolas & Pouliquen 2020). Meanwhile, the increase in cohesion also manifests macroscopically as a convex free surface with a steeper slope and thicker flowing layer, whose variations tend to saturate at high cohesion levels (Brewster *et al.* 2009; Preud'homme *et al.* 2021). Correspondingly, a higher rotation speed is required to trigger the transition from the rolling to cascading regime, reflecting the interplay and competition among inertial, cohesive and gravity-driven effects acting on the particles (Dong *et al.* 2023). Such complexity is further manifested in the particle-size dependence of the dynamic angle of repose on rotation speed. While coarse cohesive materials typically exhibit an increase in surface angle with increasing rotation speed (Jarray *et al.* 2019; Dong *et al.* 2023), the opposite trend has been reported for fine powders (e.g. particle diameter below 100 μm) (Castellanos *et al.* 1999; Neveu, Francqui & Lumay 2022), likely due to fluidisation and reduced wall friction in such systems (Pol *et al.* 2025).

Given the inherently complex dynamics of granular flows arising from the coupled effects of multiple controlling factors, it is essential to identify the governing dimensionless parameters and establish their scaling relationships. Such an approach not only enables a unified understanding of granular flow behaviour but also facilitates the scale-up from laboratory experiments to industrial and geophysical flows (Kim & Kamrin 2020; Man *et al.* 2025). While previous studies have extensively investigated this challenge, most have focused primarily on dry granular systems (Orpe & Khakhar 2001; Yang *et al.* 2008). These works have revealed that the Froude number, Fr, a dimensionless parameter representing the competition between inertial and gravitational

https://doi.org/10.1017/jfm.2026.11716 Published online by Cambridge University Press

effects, alone is insufficient to fully capture the flow dynamics, and additional system factors, such as size effects, need to be incorporated (Vu *et al.* 2024). To address this limitation, Pignatel *et al.* (2012), extending the framework of GDR MiDi (2004), proposed a representative dimensionless flow rate that has been widely adopted to characterise the flow characteristics of cohesionless particles. Similarly, Orozco *et al.* (2020) and Vu *et al.* (2024) further incorporated the filling degree J into a single scaling parameter to better capture the flow variables in the cascading regime. For cohesive granular flows, several works have examined the effects of rotation speed and cohesion on the dynamic angle of repose using dimensionless numbers such as the Weber number (Jarray *et al.* 2019), which represents the competition between inertial and capillary forces, or the Bond number in combination with Fr (Dong *et al.* 2023), which characterises the balance between cohesive and gravitational forces. In addition, recent numerical investigations using the discrete element method have proposed stiffness-dependent dimensionless formulations based on adhesive collision mechanics to describe flow regime transitions (Artoni *et al.* 2025), as well as Weber-number-based coarse-graining strategies aimed at upscaling wet granular systems while preserving macroscopic rheology (Larijani, Magnanimo & Luding 2025). Despite these efforts, few studies to date have systematically investigated the flow dynamics and scaling behaviour arising from the interplay of multiple controlling factors including cohesion, particle size and inertia, which is a practically relevant yet strongly coupled condition in granular systems that cannot be easily studied in isolation.

In this study, we aim to fill this gap through systematic drum experiments on the steady surface flow of dry and cohesive granular materials, covering a wide range of rotation speeds, drum-to-particle size ratios and cohesion strengths. A dimensionless parameter derived from dimensional analysis is proposed to capture their combined effects, and the scaling of key flow quantities with this parameter is examined to establish unified relationships across both dry and cohesive cases. The experimental methodology and dimensional formulation are described in § 2, followed by the analysis of granular flow dynamics and scaling behaviour under different conditions in § 3. Finally, § 4 concludes the paper with a summary of key findings, limitations and future perspectives.

2. Materials and methods

2.1. *Rotating drum apparatus*

A custom-built rotating drum apparatus, as illustrated in figure 2, was employed to investigate the steady surface flow dynamics of dry and cohesive granular assemblies under a broad range of flow conditions. The cylindrical sidewalls and end plates of the rotating drum are all fabricated from transparent poly-methyl methacrylate (PMMA), while a blackboard is positioned behind the drum to provide a uniform contrasting background, enabling optical access for flow visualisation and image processing. The inner PMMA walls are coated with transparent fluorinated ethylene propylene films to prevent particle adhesion. Additionally, a sealing strip is installed between the front-end plate and sidewalls to ensure drum watertightness. The drum, with a fixed inner diameter of $D = 150$ mm and a width of $W = 50$ mm, is placed vertically on a pair of parallel cylindrical rollers driven by a system-controlled stepping motor. Note that the drum width is at least 10 times the diameters d of all the particles used in this study, which exceeds the minimum requirement of $3.2d$ proposed by Jain, Ottino & Lueptow (2005), thereby ensuring that the influence of front and back wall friction on the flow dynamics can be neglected (Orpe & Khakhar 2001).

The drum, partially filled with monodisperse acrylic spheres, was rotated counterclockwise at a constant rotation speed ω. The drum rotation was precisely regulated

https://doi.org/10.1017/jfm.2026.11716 Published online by Cambridge University Press

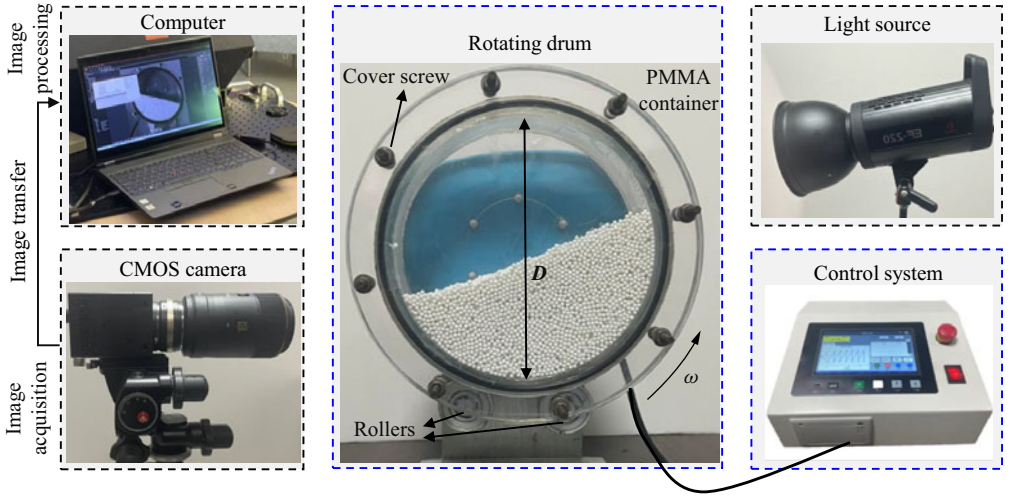


Figure 2. Experimental set-up of the rotating drum apparatus. This configuration consists of a control system that regulates a stepping motor to drive the parallel rollers, ensuring precise and stable drum rotation at a constant speed ω. A high-speed CMOS camera records the particle motion, and the captured images are transferred to a computer for subsequent image processing. In this configuration, shear within the flowing layer arises from gravity-driven surface avalanching as drum rotation continuously transports the granular material upward; no significant basal slip is observed during the present experiments. The full time-dependent evolution is provided in supplementary movie 1 is available at https://doi.org/10.1017/jfm.2026.11716.

by the control system to ensure stable operation across all cases. The spherical beads used in this study have a density of 1.20 g cm^{-3}, and five particle diameters of 2.0, 2.5, 3.0, 4.0 and 5.0 mm with a manufacturing tolerance of $\pm 2\,\%$ were employed to examine size effects on granular surface flow, which covers a variation of the drum-to-particle diameter ratios D/d with the range $30 \leq D/d \leq 75$. Monodisperse spheres were used to avoid the introduction of unnecessary parameters associated with gradation, and previous studies have shown that such packings do not induce noticeable crystallisation under low shear stresses (Chen *et al.* 2024). For each experiment, the total mass of acrylic spheres in the drum was kept constant at $m = 244.92$ g, corresponding to a consistent initial configuration with a filling level of $J \approx 0.42$ and a solid volume fraction of $\phi \approx 0.58$. Here, the filling level is calculated as the ratio $J = h_0/D$, with h_0 denoting the vertical thickness of the granular assemblies, measured from the lowest particle to the midpoint of the free surface at rest (Orozco *et al.* 2020; Vu *et al.* 2024). The rotating drum was run for 10 revolutions and more to ensure that the granular assembly reaches a steady flow state. All quantities analysed in this paper, including the particle velocity, flowing thickness and dynamic angle of repose, were averaged over the steady state.

In this study, we focus on dense granular flows within a certain range of rotation speed ω that produces continuous motion with either a flat or S-shaped free surface, namely the rolling and cascading regimes, respectively, as defined by Mellmann (2001). In both regimes, particles continuously leave the flowing layer at the lower, downslope end and are gradually transported back to the upper end, without flow intermittency (Pol *et al.* 2025). Accordingly, rotation speeds ω between 4 and 40 rpm were employed here, corresponding to Froude number Fr in the range $1.34 \times 10^{-3} \leq Fr \leq 1.34 \times 10^{-1}$. The Froude number Fr is defined as

$$Fr = \frac{\omega^2 D}{2g}, \tag{2.1}$$

https://doi.org/10.1017/jfm.2026.11716 Published online by Cambridge University Press

where g denotes the gravitational acceleration. It quantifies the relative importance of inertial and gravitational forces and is commonly used to characterise granular flow regimes, with an increase in Fr leading to a gradual transition from rolling to cascading flow (Yang *et al.* 2008). Note that in rotating drum systems, Fr serves as a global control parameter related to the rotation speed, rather than a criterion for subcritical/supercritical flow classification as in classical hydraulics. Within this context, the rolling-to-cascading transition typically occurs at $Fr \ll 1$.

During the experiments, a high-speed CMOS camera, typically operated at 1000 fps with a resolution of 1920×1080 pixels, was adopted and connected to a computer to capture the granular movements under different flow conditions. To compensate for increasingly rapid particle motions at higher drum rotation speeds, the frame rate was increased up to 1600 fps, thereby maintaining sufficient temporal resolution for reliable optical analysis. In addition, an EF-220 light source (200 W, 2700 K) directed at the drum was employed to ensure sufficient illumination for the camera. The recorded images were subsequently processed for quantitative flow analysis, as described in § 2.3.

2.2. *Interstitial fluid and capillary force*

For cohesive cases, the present study, consistent with previous works (Khamseh, Roux & Chevoir 2015; Jarray *et al.* 2019), focuses on the pendular state of low liquid contents, in which isolated liquid bridges arise at particle contacts due to the surface tension of the interstitial fluid. In this state, the attractive capillary force, nearly independent of the liquid volume at small separation distances or contact, is regarded as the primary factor distinguishing the flow dynamics of cohesive granular assemblies from that of dry particles (Halsey & Levine 1998). For two contacting particles with identical diameter d, the capillary force F_c can be expressed in the form as (Jarray *et al.* 2019; Dong *et al.* 2023)

$$F_c = \pi d \gamma \cos\theta, \tag{2.2}$$

where γ is the surface tension, and θ the liquid–solid contact angle. Under typical experimental conditions, the expression can be simplified by $F_c = \pi d \gamma$ (Nase *et al.* 2001; Pol *et al.* 2025).

For experiments under cohesive conditions, prior to being carefully poured into the drum, particles are uniformly mixed with 5.10 g of liquid, corresponding to a fluid content of 2 % by mass, to ensure that the granular assemblies remain in the pendular state (Li, Wang & Niu 2022). Note that the fluid content is fixed at $w = 2\,\%$ in this study because higher values tend to promote particle adhesion to the drum walls, which hinders particle image velocimetry measurements, whereas very low contents (e.g. 0.5 % or 1 %) make it difficult to achieve a homogeneous liquid distribution within the granular assembly, introducing experimental uncertainties. Mixtures of ethanol–water, with ethanol mass fractions C_e varying from 0 % to 15 %, are selected as the interstitial fluid in our experiments. This strategy enables precise adjustment of the surface tension γ (Jarray *et al.* 2019), a primary contributor to the capillary force F_c according to (2.2). To quantify the relative importance of this capillary-induced cohesion versus gravity, the granular Bond number Bo is employed, defined as the ratio of the maximum capillary force F_c and the weight of the particle W (Nase *et al.* 2001; Schaarsberg *et al.* 2016; Pol *et al.* 2025), given by

$$Bo = \frac{F_c}{W} = \frac{\pi d \gamma}{\frac{4}{3}\pi\,(d/2)^3\,\rho_p g} = \frac{6\gamma}{d^2 \rho_p g}, \tag{2.3}$$

where ρ_p denotes the density of the particles.

https://doi.org/10.1017/jfm.2026.11716 Published online by Cambridge University Press

Case label	d (mm)	C_e (%)	γ (mN·m^{-1})	θ (°)	Bo
CE-1	2.0	0	73.50	69.11	9.43
CE-2	2.5	—	—	—	6.03
CE-3	3.0	—	—	—	4.19
CE-4	4.0	—	—	—	2.36
CE-5	5.0	—	—	—	1.51
CD-1	2.5	0	73.50	69.11	6.03
CD-2	—	5	55.88	55.01	4.56
CD-3	—	10	45.00	41.09	3.67
CD-4	—	15	40.08	29.50	3.27

Table 1. Summary of experimental parameters for cohesive granular flows.

The experimental campaign under cohesive conditions is designed to achieve different levels of particle cohesion through two parameter sets: one varies the particle size at a fixed ethanol mass fraction in the ethanol–water mixtures ($C_e = 0\,\%$); conversely, the other varies the ethanol fraction while maintaining the particle diameter constant ($d = 2.5$ mm). The resulting combinations, together with the corresponding Bond number calculations, are summarised in table 1. Note that the contact angle θ is measured from images of liquid droplets on a PMMA plate surface using the LB-ADSA plugin in open-source imageJ software, which determines θ through fitting the Young–Laplace equation to the droplet profiles. Additionally, the surface tension values adopted are typical for room temperature and lie well within the ranges reported in previous studies (Belda, Herraez & Diez 2005; Khattab *et al.* 2012; Jarray *et al.* 2019).

As shown in table 1, in experimental cases, denoted by the symbol CD, an increase in ethanol mass fraction C_e leads to a systematic reduction in surface tension γ and the Bond number Bo, along with a decline in the contact angle θ that signals enhanced wettability of the PMMA surface. Meanwhile, for mixtures with pure water ($C_e = 0\,\%$), Bo decreases with increasing particle diameter d, spanning conditions from relatively strong to weak cohesion. The influence of Bo and particle wettability on cohesive granular flow will be examined in detail in § 3.3.

2.3. *Image processing*

Continuous image sequences of the dry and cohesive granular flows in the rotating drum are subsequently processed to extract quantitative information, including the dynamic angle of repose β_0 and particle velocity fields. Specifically, the detection of the granular bed and the measurement of the dynamic angle of repose β_0 are performed through the MATLAB Image Processing Toolbox, with the detailed procedure illustrated in figure 3. The original grey scale images (figure 3*a*) are first converted into binary images (figure 3*b*) by applying an intensity threshold, thereby segmenting solid particles (assigned a binary value of 0) from the background (binary value of 1). In this study, a threshold value of 160 is adopted to achieve the best visual representation of the granular assembly in the images. Small noise regions are then removed through area-based morphological filtering, which eliminates connected components smaller than a prescribed area threshold of 25 000 pixels. After that, the upper boundary of the granular bed (figure 3*c*) is identified by a contour detection algorithm based on Moore-neighbour tracing (Mari & Raju 2021), from which the free-surface profile is extracted and linearly fitted. Finally, the temporal evolution of β_0 is obtained by iteratively applying this procedure to each frame of the image sequence, with β_0 calculated from the best-fit line to the free surface (figure 3*d*).

https://doi.org/10.1017/jfm.2026.11716 Published online by Cambridge University Press

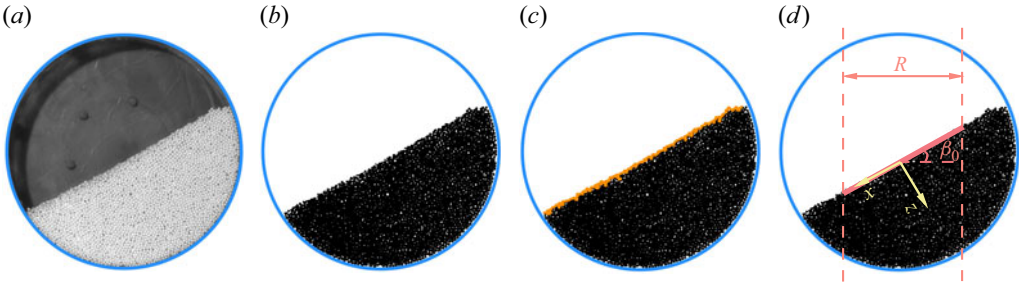


Figure 3. Detailed procedure of the image analysis for the measurement of the dynamic angle of repose β_0: (*a*) original grey scale image; (*b*) binary image after thresholding; (*c*) detected free-surface contour (orange line); (*d*) linear fitting of the free surface (pink line) for calculating β_0.

Considering the S-shaped free surface of granular flows in the cascading regime, the linear fitting of the free surface should be restricted to a limited region rather than applied to the entire surface. Accordingly, in this study, the dynamic angle of repose β_0 is measured from each binarised image over the central part of the flow surface in analogy with previous works (Jarray *et al.* 2019; Preud'homme *et al.* 2021). The fitting region spans a horizontal length R equal to half of the drum diameter D, as shown in figure 3(*d*).

The particle image velocimetry (PIV) technique is applied to successive image frames to extract the particle velocity fields. As a non-intrusive, image-based method, PIV is implemented in this study using an open-source software PIVlab (Thielicke & Sonntag 2021), where velocity fields are computed through a multi-pass cross-correlation algorithm coupled with a fast Fourier transform window deformation (Thielicke & Stamhuis 2014). The underlying principle involves dividing the region of interest into interrogation windows and calculating the displacement vector for each window by locating the peak of the cross-correlation function $r(\boldsymbol{s})$ between two consecutive frames, given by

$$r(\boldsymbol{s}) = \iint I_1(\boldsymbol{x}) \cdot I_2(\boldsymbol{x} + \boldsymbol{s})\, \mathrm{d}\boldsymbol{x}, \tag{2.4}$$

where I_1 and I_2 denote the intensity distributions of the first and second interrogation windows, respectively, with $\boldsymbol{x}$ representing the image coordinate, and $\boldsymbol{s}$ the displacement vector (Chou & Hsiau 2012).

In this study, a four-pass correlation algorithm with progressively refined interrogation windows is adopted to evaluate the recorded image frames, with a final interrogation size of 32×32 pixels selected to match the order of the particle size for reliable and robust velocity measurements. Sub-pixel displacement estimation is performed using a Gaussian 2×3-point estimator, and the overlap of the interrogation window is fixed at 50 % to enhance spatial resolution (Sanvitale *et al.* 2023). Prior to PIV analysis, the images are pre-processed using contrast-limited adaptive histogram equalisation to enhance local contrast and highlight particle features (Niu *et al.* 2024). For each experimental run, PIV analysis is performed on more than 500 consecutive images, covering over 0.5 s at 1000 fps. The resulting time-averaged particle velocity field is constructed by averaging the instantaneous velocity fields calculated from successive image pairs. The velocity distributions obtained from PIV serve as the basis for further quantitative analyses of the granular flow dynamics, such as shear rates and inertial numbers, as presented in § 3.

2.4. *Dimensional analysis of cohesive granular flows with capillary time scale*

A proper determination of the governing dimensionless parameters and associated scaling relations is crucial for achieving scale-up, the process of bridging laboratory

https://doi.org/10.1017/jfm.2026.11716 Published online by Cambridge University Press

experiments with industrial-scale granular systems. Based on a dimensional analysis of dry granular flow in a quasi-two-dimensional rotating drum, Pignatel *et al.* (2012) proposed a dimensionless flow rate as an alternative to Fr. The flow rate Q can be non-dimensionalised using a characteristic quantity with units of $[L]^2/[T]$. In granular flows, the particle diameter d is always taken as the characteristic length scale. The challenge then lies in identifying a characteristic time scale that effectively captures the relevant dynamics.

Cohesive granular flows in the pendular state can still be studied within the same dimensional framework as dry granular flows, provided that the characteristic time scale is determined to account for cohesion (Roy, Luding & Weinhart 2017). To this end, we consider the vertical balance of driving forces, including both gravity and capillary attraction, acting on an isolated cohesive particle, given by

$$\frac{4}{3}\pi\left(\frac{d}{2}\right)^3\rho_p\frac{\mathrm{d}v_p}{\mathrm{d}t}=\pi\,\mathrm{d}\gamma-\frac{4}{3}\pi\left(\frac{d}{2}\right)^3\rho_p g, \tag{2.5}$$

where v_p denotes the particle velocity. The solution of (2.5), with the initial condition $v_p\,(t=0)=0$, is given by

$$v_p\,(t)=\left(\frac{6\gamma}{d^2\rho_p}-g\right)t=g\,(Bo-1)\,t, \tag{2.6}$$

where Bo denotes the Bond number as defined in (2.3). For dry granular flows where gravity dominates ($Bo\ll 1$), the characteristic time t_d required for a single particle to travel a distance of its own diameter d is $t_d=\sqrt{d/g}$. This expression represents the time scale associated with local particle rearrangements and is consistent with that used by Pignatel *et al.* (2012). However, in the pendular state, capillary forces act as a short-range dominant interaction that determines the primary driving acceleration of particles when they are in close contact (Zhao, Kruyt & Millet 2020; Pouliquen 2025). In the limit of $Bo\gg 1$, we can obtain

$$v_p\sim g\,Bo\,t_c=\frac{d}{t_c}, \tag{2.7}$$

where t_c is the capillary time scale, expressed as

$$t_c=\sqrt{\frac{d^3\rho_p}{6\gamma}}. \tag{2.8}$$

It characterises particle motion primarily governed by the attractive capillary force (Roy *et al.* 2017). Note that the capillary force exhibits weak sensitivity to the liquid bridge volume but is strongly governed by the liquid surface tension γ. Since γ is an intrinsic material property shared by all liquid bridges in the system, the resulting capillary time scale t_c can be regarded as a global parameter.

The volumetric flow rate per unit width in a quasi-two-dimensional rotating drum can be given by

$$Q=\frac{1}{2}\omega\left[\left(\frac{D}{2}\right)^2-\delta_0^2\right]\approx\frac{1}{8}\omega D^2, \tag{2.9}$$

where δ_0 denotes the thickness of the flowing layer. The above approximation holds when the flowing layer is much thinner than the half of drum diameter D, a condition typical of the rolling regime (Ottino & Khakhar 2000). Consequently, the dimensionless flow rate

https://doi.org/10.1017/jfm.2026.11716 Published online by Cambridge University Press

for dry granular flows ($Bo \ll 1$) is defined as

$$Q_d = \frac{\frac{1}{8}\omega D^2}{d^2/t_d} = \frac{\frac{1}{8}\omega D^2}{d^2/\sqrt{d/g}} = \frac{1}{4} Fr^{1/2} \left(\frac{D}{d}\right)^{3/2}, \tag{2.10}$$

which can be reformulated for cohesive granular flows by replacing t_d with t_c to obtain

$$Q_w = \frac{\frac{1}{8}\omega D^2}{d^2/t_c} = \frac{1}{4} Fr^{1/2} \left(\frac{D}{d}\right)^{3/2} Bo^{-1/2}. \tag{2.11}$$

Therefore, the dimensionless parameter Q^*, which unifies dry, gravity-driven flows ($Bo \ll 1$) and pendular-state cohesive granular flows dominated by capillary forces ($Bo \gg 1$), can be expressed as

$$Q^* = \begin{cases} \dfrac{1}{4} Fr^{1/2} \left(\dfrac{D}{d}\right)^{3/2}, & Bo \ll 1, \\ \dfrac{1}{4} Fr^{1/2} \left(\dfrac{D}{d}\right)^{3/2} Bo^{-1/2}, & Bo \gg 1. \end{cases} \tag{2.12}$$

The expressions in (2.12) originate from a simplified force-balance analysis on an isolated particle. Although idealised, this approach has been successfully applied to diverse granular flow configurations (Courrech du Pont *et al.* 2003; Pignatel *et al.* 2012) and, as shown below, also provides a valuable framework for analysing our experimental observations. In addition, it should be noted that while the expression of Q^* in cohesive cases represents a theoretical limit for $Bo \gg 1$, the transition from gravity-driven to capillary-dominated flow fundamentally occurs as Bo surpasses 1 (Pouliquen 2025). For the Bond numbers investigated in the cohesive cases of this study, the capillary forces are sufficiently dominant to justify this asymptotic scaling approach. Meanwhile, in the cross-over regime between these two asymptotic limits, a wet–dry transition may occur where both gravity and cohesion contribute comparably to the flow; however, this regime is beyond the scope of the present study.

3. Results and discussion

3.1. *Characterisation of particle velocities in dry flows*

3.1.1. *Flow regimes and spatial velocity distributions*

For the dry cases, two representative snapshots of the averaged particle velocity vectors in drums with different Froude numbers Fr but identical size ratio $D/d = 60$ are displayed in figure 4. These vector fields provide a global kinematic overview of the granular flow, capturing the overall transport of granular materials within the rotating drum. It can be observed that an increase in Fr from 1.34×10^{-3} to 7.55×10^{-2} induces a clear transition of the flow regime from rolling to cascading, characterised by the evolution of the free surface from a nearly linear profile into an S-shaped curvature. Meanwhile, the particle velocity magnitude in the rotating drum, indicated by the arrow lengths, increases significantly with Fr, especially in the vicinity of the free surface and along the drum wall. In both cases, the largest velocities occur at the centre of the free surface where particles flow downward in a counterclockwise direction, and the velocity gradually decays inward to 0 at the vortex core. Near the drum wall, the flow exhibits a rigid-body motion synchronised with the drum rotation, continuously lifting and transporting particles to the upper region of the drum.

https://doi.org/10.1017/jfm.2026.11716 Published online by Cambridge University Press

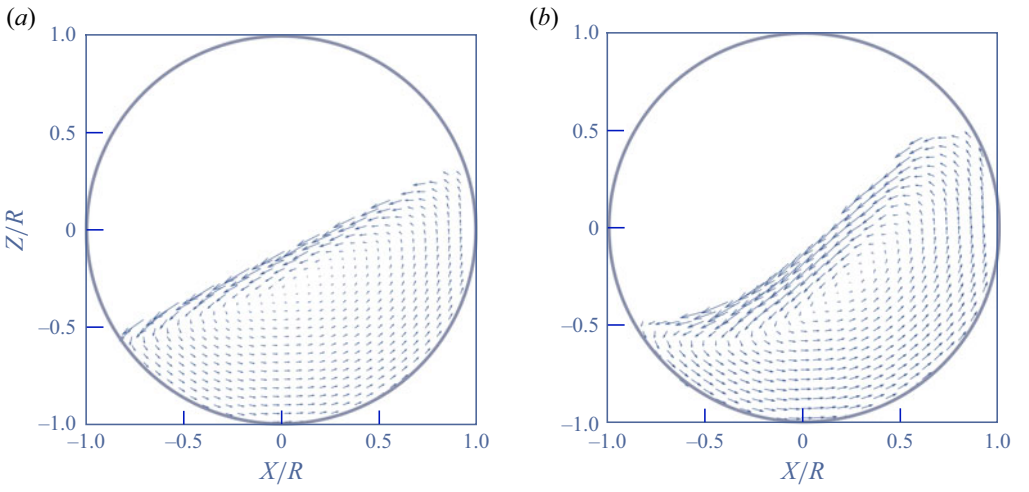


Figure 4. Velocity vector fields for dry granular flows in a rotating drum at different rotation speeds: (*a*) $\omega =$ 4 rpm ($Fr = 1.34 \times 10^{-3}$); (*b*) $\omega = 30$ rpm ($Fr = 7.55 \times 10^{-2}$). In both cases, the particle diameter is fixed to 2.5 mm ($D/d = 60$). Arrow length is scaled with the particle velocity magnitude.

In both rolling and cascading regimes, the velocity in the central region near the free surface, spanning a horizontal length of R as shown in figure 3(*d*), is nearly parallel to the surface. Therefore, to ensure the velocity components have a physically intuitive representation of the actual flow process, we introduce a Cartesian coordinate system (x, z) with its origin at the centre of the free surface. Here, the x axis is oriented parallel to the local downward flow, while the z axis is defined normal to the surface flow and directed into the granular bed. The transformation between the (x, z) and the global (X, Z) coordinate system is given by

$$\begin{pmatrix} x \\ z \end{pmatrix} = \begin{pmatrix} -\cos\beta_0 & -\sin\beta_0 \\ \sin\beta_0 & -\cos\beta_0 \end{pmatrix} \begin{pmatrix} X \\ Z \end{pmatrix}, \tag{3.1}$$

where β_0 is the dynamic angle of repose measured in the global coordinate system (X, Z).

Based on this streamwise-oriented coordinate system, we compare the time-averaged fields of the x-component of particle velocity $\langle u \rangle$ in rotating drums with various size ratios D/d and Froude numbers Fr, as displayed in figure 5. Positive $\langle u \rangle$ values correspond to the gravity-driven downward granular flow, while negative values indicate the upward transport of particles driven by drum rotation. Figure 5 shows that for drums with a fixed D/d, an increase in Fr leads to higher $\langle u \rangle$ values near the free surface and an expansion of the downward flow region, which is accompanied by a gradual transition from rolling to cascading regime, consistent with the observations in figure 4. Specifically, the transition to the cascading regime is observed at $Fr \approx 10^{-3}$–10^{-2} in our study, which is in good agreement with the critical values reported in previous literature (Mellmann 2001; Preud'homme *et al.* 2021). However, at a constant Fr, the high-velocity area within the downward flow systematically contracts as the size ratio D/d decreases, exemplified at $Fr = 7.55 \times 10^{-2}$ by the noticeable reduction in the area where $\langle u \rangle$ is larger than 0.4 m s^{-1}. In addition, as illustrated in figure 5(*e*), the evolution of free-surface profiles with Fr reveals a delayed transition from the rolling to the cascading regime compared with cases with larger D/d. This indicates that larger particles, corresponding to a smaller D/d, require higher rotation speeds to trigger this transition, since their greater individual inertia combined with reduced particle contacts hinders the collective onset of cascading

https://doi.org/10.1017/jfm.2026.11716 Published online by Cambridge University Press

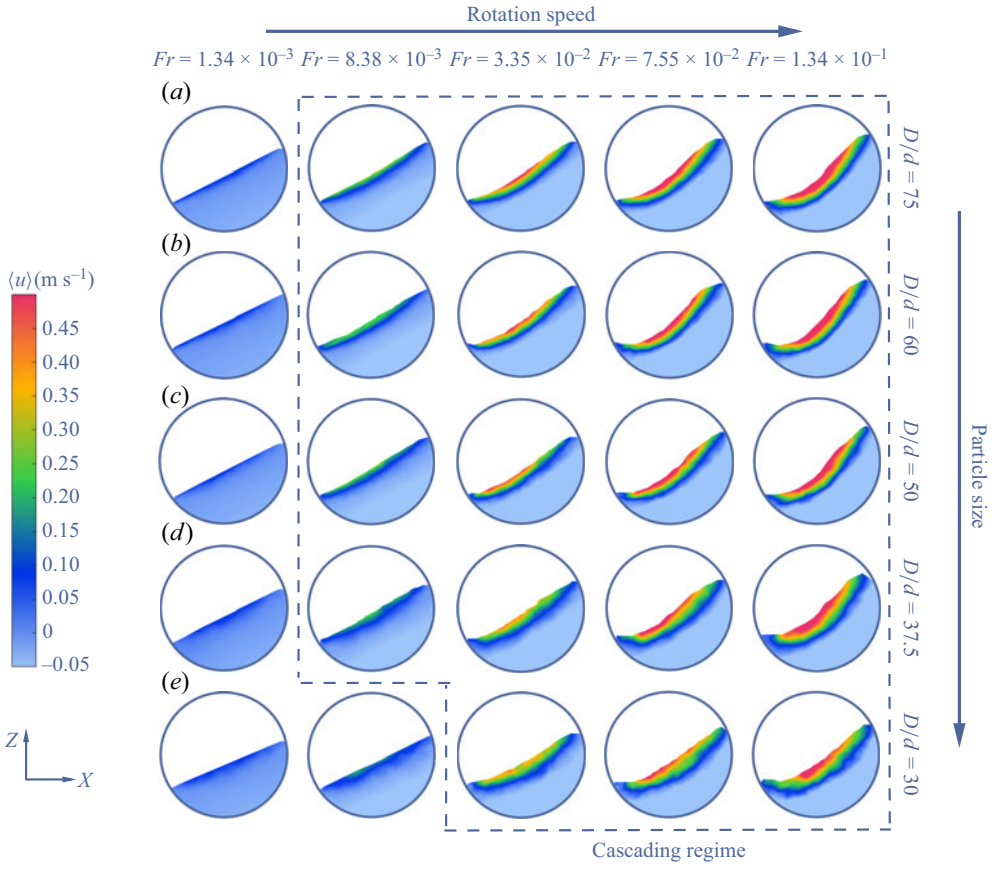


Figure 5. Time-averaged fields of the x-component of particle velocity $\langle u\rangle$ in rotating drums with different size ratios D/d and Froude numbers Fr: panels show (*a*) $D/d = 75$; (*b*) $D/d = 60$; (*c*) $D/d = 50$; (*d*) $D/d = 37.5$; (*e*) $D/d = 30$. For a fixed D/d, the Fr increases from 1.34×10^{-3} to 1.34×10^{-1} from left to right. The cases enclosed by dashed lines correspond to conditions that have visually transitioned into the cascading regime, and the colour of granular bed represents the $\langle u\rangle$ values.

(Dong *et al.* 2023). The dependence on D/d, despite a constant Fr, demonstrates that Fr is not the sole parameter controlling the granular flow dynamics in rotating drums, as will be discussed in more detail below.

To gain further quantitative insight into the flow dynamics, we extracted the profile of the time-averaged velocity $\langle u\rangle$ in the x-direction as a function of depth z, measured from the free surface, in a rotating drum with fixed $Fr = 3.35 \times 10^{-2}$ and $D/d = 60$, as shown in figure 6(*a*). The open symbols and solid line represent the results of our PIV measurements and corresponding theoretical velocity $u = -\omega z'$ for the rigid rotation following the rotating drum, respectively. Here, z' denotes the depth measured from the drum centre. Both the measured $\langle u\rangle$ and theoretical u velocities decrease with depth z. A pronounced deviation from rigid rotation is observed near the free surface, whereas $\langle u\rangle$ converges toward the theoretical profile of u beyond a depth of $z > 0.03$ m, which to an extent provides a validation of our PIV measurements. In addition, a new quantity, $\langle u_x\rangle = \langle u\rangle - u$, is introduced to describe the particle velocity relative to the rigid rotation of the drum, with the rotation speed subtracted from $\langle u\rangle$ values obtained from PIV. This approach effectively facilitates a clearer characterisation of the intrinsic dynamics

https://doi.org/10.1017/jfm.2026.11716 Published online by Cambridge University Press

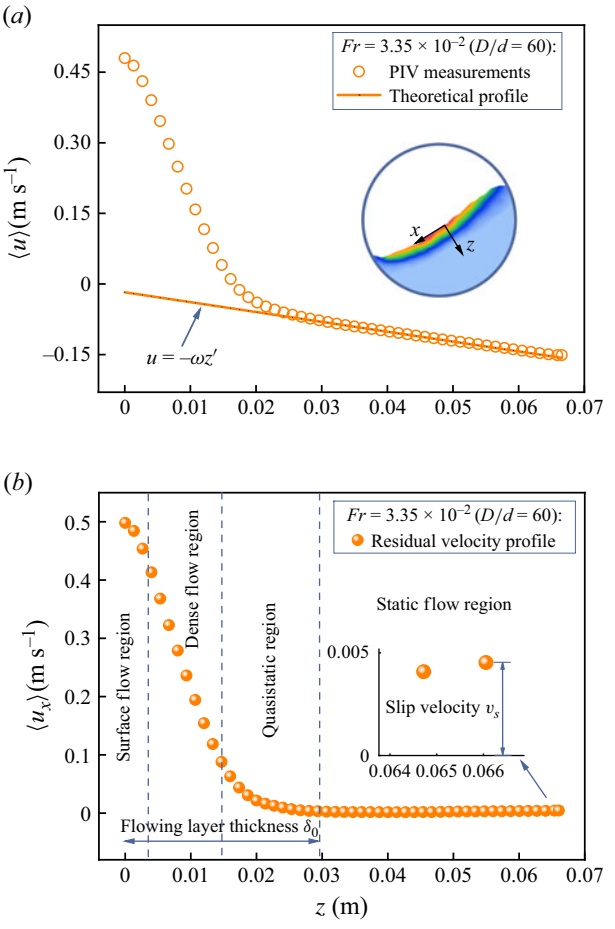


Figure 6. Profiles of (*a*) the time-averaged velocity $\langle u \rangle$ and (*b*) the particle velocity $\langle u_x \rangle$ as functions of depth z in a rotating drum with a fixed $Fr = 3.35 \times 10^{-2}$ and $D/d = 60$. The depth is measured from the free surface, as shown in the inset of (*a*). The solid line represents the corresponding theoretical velocity u for rigid rotation of the drum, given by $u = -\omega z'$, where z' denotes the depth measured from the drum centre. The quantity $\langle u_x \rangle = \langle u \rangle - u$ represents the particle velocity relative to the rigid rotation of the drum.

of particle motion, consistent with prior studies (Hill, Gioia & Tota 2003; Li & Andrade 2020).

Figure 6(*b*) presents the profile of the time-averaged particle velocity $\langle u_x \rangle$ along the depth in the z direction, which gradually decreases and eventually plateaus near zero. Based on the evolution of this profile, four distinct regions can be distinguished along the depth: the surface flow, the dense flow, the quasistatic and the static flow regions. Starting from the top of the surface flow region, the particle velocity $\langle u_x \rangle$ reaches its maximum, and particle interactions are dominated by collisions, especially in cascading flows. Moving into the dense flow region, $\langle u_x \rangle$ exhibits a nearly linear decay with depth. This linear scaling implies a nearly constant shear rate, characteristic of friction-dominated regimes. It reflects a balance between gravitational driving stress and internal frictional resistance within a densely packed flowing layer, consistent with the established observations in rotating drum studies (Rajchenbach 1990; Bonamy *et al.* 2002; GDR MiDi 2004; Li & Andrade 2020). Approaching the bottom of the flowing layer, the decay of $\langle u_x \rangle$ transitions from linear to exponential-like, marking the onset of the quasistatic

https://doi.org/10.1017/jfm.2026.11716 Published online by Cambridge University Press

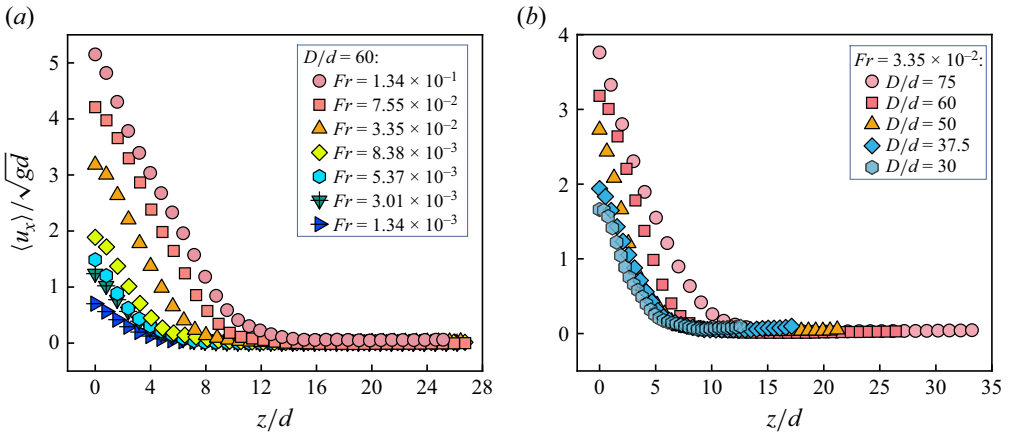


Figure 7. Profiles of the time-averaged particle velocity $\langle u_x \rangle$ normalised by $\sqrt{gd}$, plotted as a function of the normalised depth z/d. (*a*) Effect of Fr at $D/d = 60$; (*b*) effect of D/d at $Fr = 3.35 \times 10^{-2}$.

region, where particle motion becomes extremely slow and interactions are predominantly governed by enduring frictional contacts (Govender 2016). Beneath the quasistatic region lies the static flow region, where the flow is essentially static relative to the rotating drum, although a minor slip at the drum wall persists, as shown in the inset of figure 6(*b*).

Next, the dependence of the time-averaged particle velocity $\langle u_x \rangle$ profiles along the depth z on the Froude number Fr and the size ratio D/d is investigated, where $\langle u_x \rangle$ is normalised by $\sqrt{gd}$ and z by the particle diameter d, as displayed in figure 7. For a drum with a fixed $D/d = 60$ across a wide range of Fr spanning the rolling and cascading regimes, an increase in Fr significantly enhances both the magnitude and slope of $\langle u_x \rangle(z)$ within the dense flow region (figure 7*a*), indicating intensified particle collisions and stronger fluidisation in the vicinity of the free surface. In addition, the slip velocity at the drum wall also increases with Fr, primarily due to the enhanced centrifugal and lift forces that promote particle detachment from the wall and thereby increase the overall mobility of the flowing layer. In figure 7(*b*), the velocity profiles for various values of D/d at a fixed $Fr = 3.35 \times 10^{-2}$ are shown. As D/d increases, both the surface velocity and the velocity gradient within the flowing layer become more pronounced, accompanied by a reduction in slip velocity. This size effect indicates that larger D/d corresponds to a higher particle feed rate at the upstream end of the free surface, resulting in a thicker flowing layer as well as a more curved free-surface profile (Orozco *et al.* 2020), as evidenced in figure 5.

3.1.2. *Flowing layer thickness*

In a rotating drum, the dominant physical mechanisms are primarily confined to the flowing layer, a region characterised by its thickness δ_0, which provides a basis for estimating the order of magnitude of other critical kinematic quantities, such as the mean velocity and shear rate (Pignatel *et al.* 2012). Following the approach of Jarray *et al.* (2019), δ_0 is defined as the depth from the free surface to the boundary of the quasistatic region, as shown in figure 6(*b*). Here, this boundary is determined from the $\langle u_x(z) \rangle$ profile where $\langle u_x \rangle$ falls below 1 % of its maximum value at the free surface. Note that although various methods for estimating the flowing layer thickness have been reported in previous studies (Pignatel *et al.* 2012; Orozco *et al.* 2020), the choice of δ_0 definition has been shown to have little effect on the qualitative scaling behaviour, as discussed in Félix *et al.* (2007). This is attributed to the self-similar scaling structure of the velocity profile, which

https://doi.org/10.1017/jfm.2026.11716 Published online by Cambridge University Press

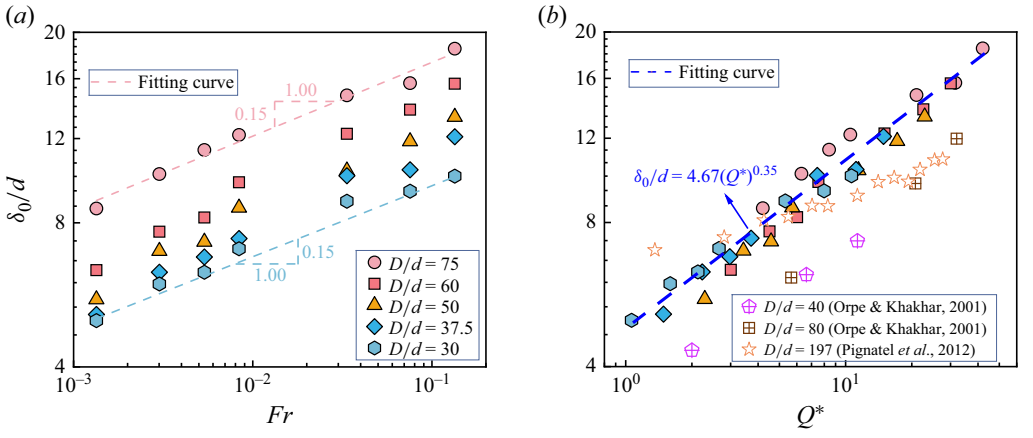


Figure 8. Normalised flowing layer thickness δ_0/d as a function of (*a*) the Froude number Fr and (*b*) the scaling parameter Q^* defined in (2.12) for different values of the size ratio D/d. The dashed lines represent the correlations fitted to our experimental data.

ensures that modifying the boundary effectively rescales the thickness without altering its dependence on control parameters, including Fr and D/d. Detailed derivations supporting this argument can be found in Oba & Otsuki (2026).

Figure 8(*a*) shows the normalised flowing thickness δ_0/d plotted against the Froude number Fr for different size ratios D/d. For a fixed D/d, δ_0/d scales with Fr as a power law with an exponent of approximately 0.15. Meanwhile, δ_0/d exhibits a clear positive dependence on D/d, indicating that Fr alone cannot fully govern the granular flow dynamics in rotating drums. This dependence is primarily attributed to the reduced influence of end-wall effects and lateral confinement at higher D/d, which promotes the development of a thicker shear zone (Bonamy *et al.* 2002). Therefore, the effect of D/d should be considered together with Fr when characterising the flow behaviour.

As introduced in § 2.4, the dimensionless flow rate for dry cases, given by $Q^* = Fr^{1/2}(D/d)^{3/2}/4$, provides an alternative approach to scaling the experimental data. It can be clearly seen from figure 8(*b*) that most data points of δ_0/d as a function of Q^* collapse onto a unified curve, irrespective of the rotation speed or particle size, with a coefficient of determination (R^2) of 0.96. The data follow a power-law relationship similar to that observed when δ_0/d is plotted against Fr, but with a larger exponent of 0.35 and a significantly better overall collapse. To validate the robustness of the δ_0/d–Q^* scaling law for dry cases in this study, experimental data from Orpe & Khakhar (2001) and Pignatel *et al.* (2012) are also plotted in figure 8(*b*) for comparison. Given that the definition of δ_0 and particle properties differ among these studies, which mainly affect the prefactor rather than the qualitative scaling behaviour, the comparison therefore focuses on the scaling exponent. As shown in figure 8(*b*), the present scaling exponent ($n = 0.35$) is higher than the value of 0.15 reported by Pignatel *et al.* (2012). This discrepancy is likely attributed to the fact that n is not a universal constant but depends on the range of Q^* explored and the flow regime (Pignatel *et al.* 2012). While the Q^* ranges are comparable, the datasets in Pignatel *et al.* (2012) are restricted to the rolling regime characterised by nearly flat free surfaces, whereas our experiments span both rolling and cascading regimes. The development of pronounced S-shaped free-surface profiles in the cascading regime leads to a steeper scaling response. Our interpretation is further supported by Orpe & Khakhar (2001), whose experiments also involved cascading flows and yielded an exponent of 0.31, close to the present value of 0.35 within a similar Q^* range.

https://doi.org/10.1017/jfm.2026.11716 Published online by Cambridge University Press

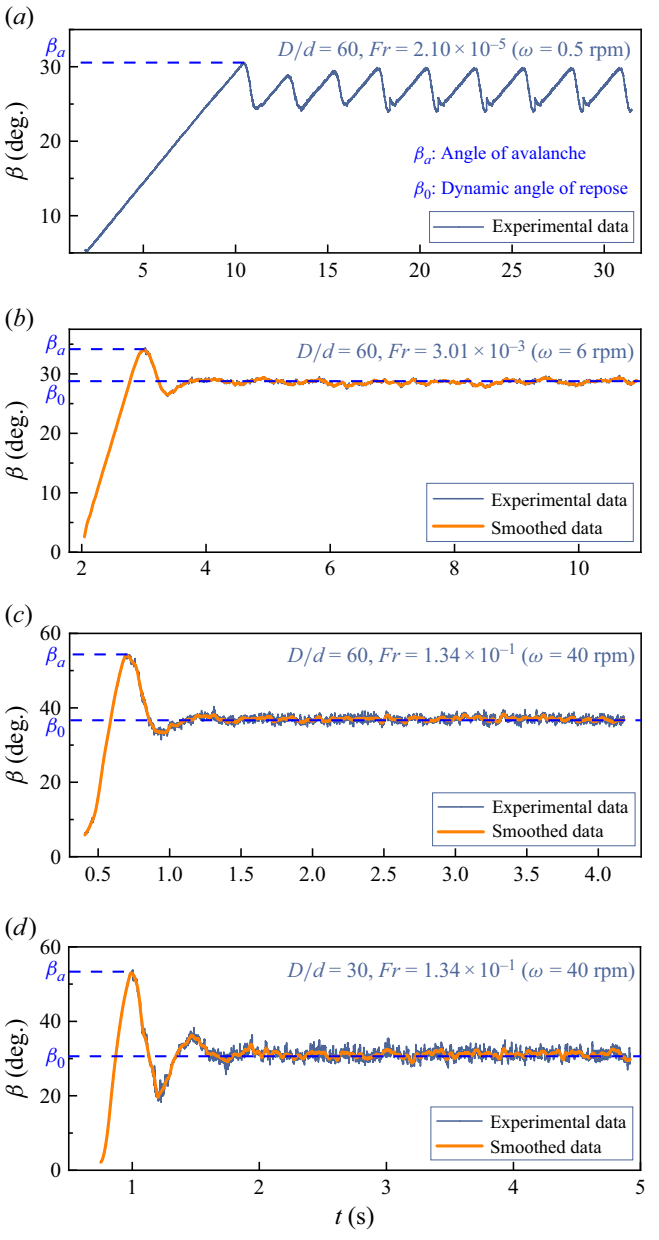


Figure 9. Temporal evolution of the free-surface angle β at a fixed size ratio of $D/d = 60$ under different Froude numbers: (*a*) $Fr = 2.10 \times 10^{-5}$; (*b*) $Fr = 3.01 \times 10^{-3}$; (*c*) $Fr = 1.34 \times 10^{-1}$. Panel (*d*) shows the case with the same Fr as in (*c*) but with a smaller size ratio $D/d = 30$, highlighting the effect of D/d on the surface profile. The experimental data are fitted by a smoothing spline shown in orange.

3.2. *Free surface in dry granular flows*

3.2.1. *Dynamic angle of repose*

A simple yet effective characterisation of the macroscopic surface morphology of granular flows can be achieved through the free-surface angle β (Zhao *et al.* 2018), which reflects the dynamic balance between gravitational driving and internal resistance forces within the flowing layer. Figure 9 presents the temporal evolution of the free-surface angle β for

https://doi.org/10.1017/jfm.2026.11716 Published online by Cambridge University Press

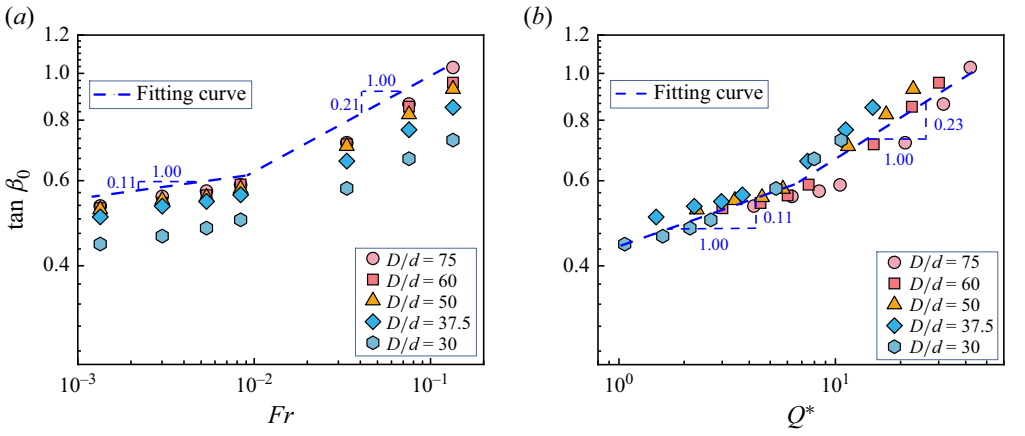


Figure 10. The tangent of the dynamic angle of repose tan β_0 as a function of (*a*) the Froude number Fr and (*b*) the scaling parameter Q^* defined in (2.12) for dry cases with different values of the size ratio D/d. The dashed lines represent the fitted correlations.

different values of the Fr and D/d. At an extremely low rotation speed of $\omega = 0.5$ rpm shown in figure 9(*a*), β increases linearly with time as particles gradually lifted to the upper part of the drum until reaching the critical stable inclination angle, called the angle of avalanche β_a (Marteau & Andrade 2018). Once β exceeds this threshold, an avalanche is released with a downslope fluid-like flow suddenly happening, accompanied by a linear drop in β until the lowest energy is reached. Further rotation triggers successive avalanches, and this periodic behaviour signifies the occurrence of the slumping regime (Mellmann 2001), which is beyond the scope of the present study. As the rotation speed increases to 6 rpm, the free surface eventually stabilises after an avalanche at the dynamic angle of repose β_0, indicating that the flow reaches a continuous state, as displayed in figure 9(*b*). When the flow transitions into the cascading regime ($Fr = 1.34 \times 10^{-1}$ in figure 9*c*), β_0 becomes larger and exhibits more pronounced temporal fluctuations during the continuous steady state. This is because higher rotation speeds amplify particle inertia and collisional interactions, leading to a steeper free surface and a higher degree of disorder in surface particle motion. In addition, as shown in figure 9(*d*), a smaller size ratio D/d induces a decisive, large-scale avalanche, following which the free surface stabilises in the steady state characterised by larger surface fluctuations and a lower β_0, compared with the case in figure 9(*c*) at the same Fr. The underlying mechanism involves the facilitated shear accommodation of larger particles through more frequent rolling and rearrangement, which reduces the effective internal friction and enables stable flow at a gentler slope.

Given the observed temporal fluctuations of the free surface, the dynamic angle of repose β_0 is computed by averaging the surface angles identified in each frame throughout the steady-state period. Its tangent, tan β_0, which is commonly used to characterise the flow dynamics, is then plotted as a function of the Froude number Fr and the scaling parameter Q^* for different size ratios D/d, as shown in figures 10(*a*) and 10(*b*), respectively. Globally, for a constant D/d, tan β_0 increases systematically with Fr, following a two-stage power-law behaviour consistent with previous work (Preud'homme *et al.* 2021). The slope in the log–log plot changes from 0.11 to 0.21 at $Fr = 8.38 \times 10^{-3}$, marking the transition from the rolling to the cascading regime. The observed two-fold increase in the growth rate of tan β_0 in the cascading regime can be fundamentally attributed to the shift to a more efficient energy dissipation mechanism (Vu *et al.* 2024). In this regime,

https://doi.org/10.1017/jfm.2026.11716 Published online by Cambridge University Press

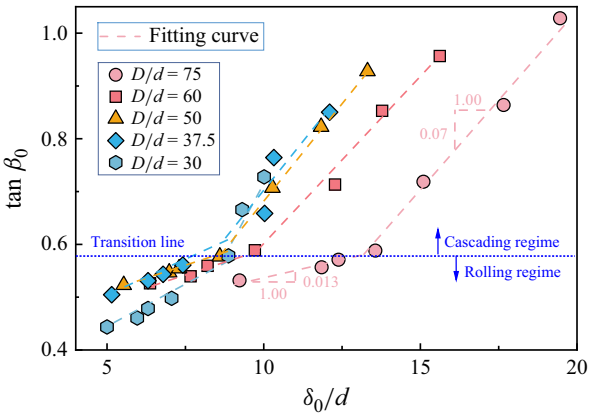


Figure 11. Relationships between the tangent of the dynamic angle of repose tan β_0 and the normalised flowing layer thickness δ_0/d for different size ratios D/d. The dashed lines correspond to linear fits, and the dotted line marks the transition from the rolling to the cascading regime.

particles experience more frequent collisions and longer trajectories along the S-shaped free surface, leading to an enhanced internal energy dissipation. To maintain a steady flow, the system must establish a steeper dynamic angle of repose, thereby providing sufficient gravitational driving force to balance this enhanced internal resistance. Consequently, the enhanced inertial effects make tan β_0 more sensitive to changes in Fr, leading to a faster growth compared with the rolling regime.

The data in figure 10(*a*) also reveal a clear dependence of tan β_0 on the size ratio D/d at a given Fr, with smaller D/d corresponding to a lower tan β_0. This trend is most pronounced for $D/d = 30$ due to size effects. To incorporate this dependence, the evolution of tan β_0 is plotted against the scaling parameter Q^* in figure 10(*b*). Similarly, figure 10(*b*) clearly exhibits a piecewise power-law growth, with exponents of 0.11 and 0.23 separated by a critical threshold at $Q^* \approx 8$. This behaviour indicates that the increase in inertial effects with Q^* leads to a transition in the dominant particle interaction mechanisms. The introduction of Q^*, however, leads to a markedly improved data collapse across all values of D/d and Fr, with most data following a universal two-stage scaling relation. This further demonstrates that the scaling parameter Q^* is a governing dimensionless parameter capable of predicting and controlling the dry granular flow based on the particle size ratio and operational Froude number.

3.2.2. *Relationship between the surface angle and flowing layer thickness*

Particular attention is directed to the correlation between the surface profile, as a kinematic feature, and the flowing layer thickness, which reflects the flow dynamics. Figure 11 presents the tangent of the dynamic angle of repose tan β_0 as a function of the normalised flowing layer thickness δ_0/d for different size ratios D/d. For a given D/d, tan β_0 exhibits a piecewise linear growth with δ_0/d, characterised by a significantly steeper slope in the second stage, reflecting intensified particle collisions and momentum transfer typical of the cascading regime; for instance, the slope increases from 0.013 to 0.07 for the case of $D/d = 75$. Interestingly, the transition between the two stages of linear growth consistently occurs at a critical angle, tan $\beta_0 \approx 0.58$, irrespective of Fr and D/d, which can be interpreted as a turning point from the rolling and cascading regimes. This observation is in good agreement with the visual evidence of the free-surface morphologies shown

https://doi.org/10.1017/jfm.2026.11716 Published online by Cambridge University Press

in figure 5 and corresponds to the rolling-to-cascading transition identified in figure 10, providing a promising criterion for distinguishing the onset of regime transition.

Another interesting observation is that the slope k in each stage systematically increases with decreasing D/d, indicating an enhanced sensitivity of $\tan\beta_0$ to δ_0/d. The relationship between $\tan\beta_0$ and δ_0/d in the first stage, corresponding to the rolling regime, can be expressed as

$$\tan\beta_0 = k_1\,(\delta_0/d) + b_1, \tag{3.2}$$

where b_1 is the fitting parameter that depends on the size ratio, exhibiting an increasing trend with D/d. A similar linear form describing the relationship between the surface angle and the flowing layer thickness was also reported by Pignatel *et al.* (2012). Based on a static friction force balance, they related the slope k_1 to an effective Coulombic friction parameter μ_w, serving as a macroscopic measure of particle–wall interactions. From this perspective, larger particles, associated with higher values of k_i and consequently greater effective Coulombic friction against the sidewalls, experience stronger lateral confinement, thereby requiring higher rotation speeds to achieve a comparable flow dynamics. This provides a physical explanation for the increase in δ_0/d with larger D/d at a given surface angle, as shown in figure 11. In addition, the intercept b_1 physically represents the macroscopic resistance to flow initiation, which can be associated with the effective friction μ_s between the moving particles and the static granular bed (Pignatel *et al.* 2012). As D/d increases, smaller particles form more contacts with the fixed granular bed, resulting in a higher μ_s and thereby necessitating a steeper surface angle to overcome these interactions and initiate flow (Zhang *et al.* 2025).

Considering the good agreement between the physical interpretation of the friction coefficients and our experimental observations, equation (3.2) can be rewritten as

$$\tan\beta_0 = \mu_w\,(\delta_0/d) + \mu_s. \tag{3.3}$$

This relationship represents a force balance between the gravitational driving force and the frictional resistance from the sidewalls and the static granular bed, effectively capturing the granular flow dynamics through the macroscopic friction coefficients μ_w and μ_s, which vary systematically with the size ratio D/d.

When transitioning into the cascading regime, the relationship between $\tan\beta_0$ and δ_0/d is given by

$$\tan\beta_0 = k_2\,(\delta_0/d - b_2) + C, \tag{3.4}$$

where $C \approx 0.58$ denotes the critical angle marking the rolling–cascading transition. In this regime, k_2 can still be interpreted as an effective Coulombic friction parameter μ_w due to the enhanced wall friction. However, once the flow fully enters the inertia- and collision-dominated cascading regime, b_2 no longer reflects a direct measure of macroscopic friction between particles and the static bed. Instead, it acts primarily as a fitting offset characterising the threshold thickness of the flowing layer required for the transition into the cascading regime. As b_2 increases systematically with D/d, larger values of D/d correspond to a thicker flowing layer involving a greater fraction of mobilised particles and stronger collisional interactions, leading to more pronounced inertial flow behaviour.

3.3. *Flow dynamics and scaling behaviour of cohesive granular materials*

3.3.1. *Effect of size ratio*

Having characterised the flow dynamics of dry granular materials, attention is now directed to cohesive granular systems obtained by introducing a small amount of liquid, which transforms the assembly into a pendular state. The presence of interstitial liquid

https://doi.org/10.1017/jfm.2026.11716 Published online by Cambridge University Press

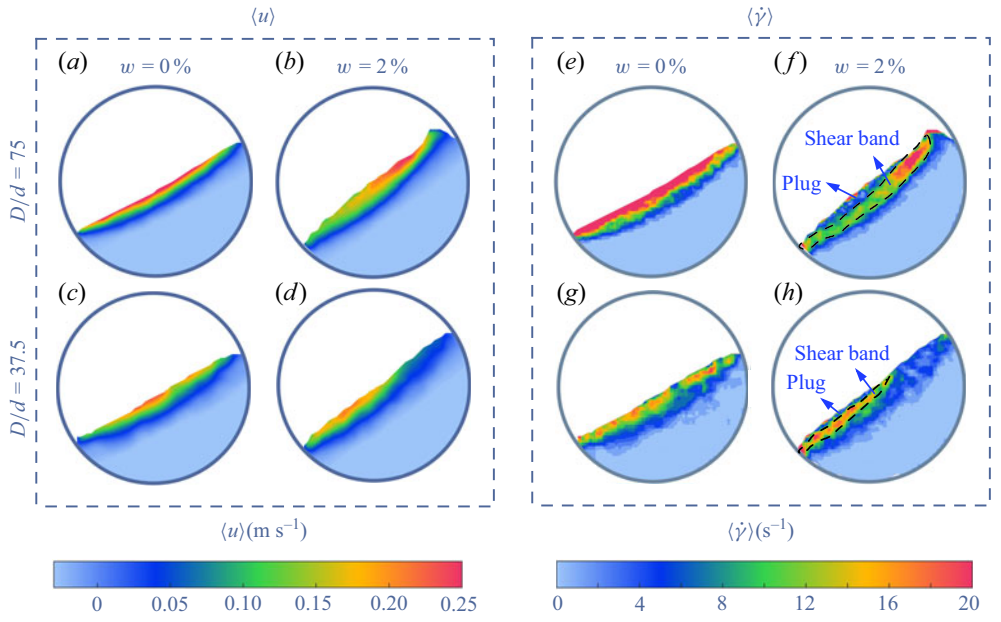


Figure 12. Time-averaged fields of particle velocity $\langle u \rangle$ (*a–d*) and shear rate $\langle \dot{\gamma} \rangle$(*e–h*) in rotating drums with different size ratios D/d (75 and 37.5) and liquid contents w (0 % and 2 %). The rotation speed is fixed at $\omega = 10$ rpm ($Fr = 8.38 \times 10^{-3}$). The region enclosed by the black dashed line denotes the shear band, while the area between this band and the free surface corresponds to the plug zone.

generates capillary bridges between particles, giving rise to cohesive interactions that significantly change the overall flow dynamics (Pol *et al.* 2025). To illustrate these effects, cohesive particles with pure water as the interstitial fluid are first examined in rotating drums at a liquid content of $w = 2\,\%$ and a rotation speed of $\omega = 10$ rpm ($Fr = 8.38 \times 10^{-3}$). Two representative particle size ratios ($D/d = 75$ and 37.5) are considered, and the corresponding surface morphologies and particle velocity fields are shown in figures 12(*b*) and 12(*d*), with the dry counterparts presented in figures 12(*a*) and 12(*c*) for comparison.

It can be clearly seen that the addition of pure water leads to a larger dynamic angle of repose β_0 for both size ratios with respect to the cohesionless cases. For $D/d = 75$, the free surface of the cohesive granular material exhibits a more convex profile (figure 12*b*), accompanied by the appearance of particle clusters formed through liquid bridges and the associated capillary forces. These cohesive clusters enhance the internal shear resistance of the flowing layer, demanding a steeper surface to sustain steady flow. When D/d in the cohesive granular system decreases to 37.5, corresponding to a reduction in Bo from 9.43 to 2.36, the free surface becomes smoother with a smaller β_0, and the clustering effect weakens (figure 12*d*). This behaviour is attributed to the reduced dominance of capillary over gravitational forces, implying a weaker cohesion effect. Therefore, at a given rotation speed, smaller particles experience stronger relative capillary cohesion, which efficiently resists shear and allows them to be transported further up the drum wall, resulting in a steeper surface slope. A similar dependence of the surface angle on particle size has been reported in previous studies on cohesive granular systems (Nowak, Samadani & Kudrolli 2005; Liu, Yang & Yu 2011). In addition, the surface flow velocity decreases when cohesion is introduced, primarily because capillary bridges strengthen interparticle forces that hinder particle sliding, while the kinetic energy is

https://doi.org/10.1017/jfm.2026.11716 Published online by Cambridge University Press

further dissipated through cohesive interactions between partially saturated particles. Compared with smaller cohesive particles, larger particles possess weaker capillary bridges that are prone to continuous rupture and reformation under shear, resulting in pronounced hysteretic energy dissipation and consequently a reduced surface velocity under identical rotational speed. This highlights the coupled roles of inertial and capillary forces in governing cohesive granular flow.

By visual inspection of the particle velocity fields, the flowing layer thickness exhibits an increasing trend with cohesion. To further understand the underlying particle movement mechanisms within this expanded flowing region, the time-averaged fields of the local shear rate $\langle\dot{\gamma}\rangle$ are analysed, as shown in figure 12(*e–h*). Here, the shear rate $\dot{\gamma}$ is calculated as

$$\dot{\gamma} = \frac{1}{2}\left(\frac{\partial u}{\partial z} + \frac{\partial v}{\partial x}\right), \tag{3.5}$$

where u and v denote the particle velocities in the directions parallel and normal to the free surface, respectively, defined in the local streamwise coordinate system (x, z). The symmetric form of the rate-of-strain tensor in (3.5) is employed to inherently exclude the contribution of rigid-body rotation, ensuring that the calculated shear rate reflects only the intrinsic deformation of the granular bed. This approach is consistent with established practices in recent granular flows studies (Dong *et al.* 2023; Chen *et al.* 2024).

In contrast to the cohesionless cases, where high shear rates are localised near the free surface, the presence of cohesion leads to a distinct stratification of the flowing layer into an upper plug zone and a lower shear band, as shown in figure 12(*f*). Within the plug zone, the shear rate approaches zero, indicating collective particle motion in the form of quasi-rigid clusters with negligible internal deformation (Preud'homme *et al.* 2021; Wang *et al.* 2023). The change in the surface flow region signifies a transition from a collisional to a viscoplastic regime, where the dominance of capillary forces strengthens interparticle bonding and enhances energy dissipation, leading to reduced shear rates and less intensive deformation in both the plug zone and the shear band. In addition, with a decrease in D/d, both the plug zone and the shear band become narrower, and the shear rates within these regions decline (figure 12*h*), indicating that the flow gradually approaches a collisional regime as the relative cohesion effect becomes less significant. This variation in flowing layer thickness reflects the competition between cohesive and inertial forces, where stronger cohesion effects enhance interparticle coupling and facilitate stress transmission over a greater depth, thereby extending the sheared region.

To provide a quantitative insight into how cohesion affects the velocity distribution within the flowing layer, the profiles of the time-averaged particle velocity $\langle u_x\rangle/\sqrt{gd}$ along the depth are investigated for dry and cohesive cases with different particle size ratios D/d under a fixed rotation speed of $\omega = 10$ rpm, as presented in figure 13. The velocity profiles for cohesive cases exhibit a slower decrease with depth compared with the dry cases, resulting in a more flattened and stretched shape and a thicker flowing layer. This reflects a reduced shear rate within the flowing layer, which arises from the formation of particle clusters induced by interparticle cohesion, consistent with the observations in figure 12. From a classical hydraulic perspective, the normalised velocity $\langle u_x\rangle/\sqrt{gd}$ can be interpreted as a local Froude number Fr_{local} (Yang *et al.* 2020), where $Fr_{local} > 1$ and $Fr_{local} < 1$ correspond to supercritical and subcritical flow states, respectively. Note that, while the surface flow in dry cases remains predominantly supercritical, the introduction of cohesion significantly suppresses the flow intensity. For instance, in cases with $D/d = 50$ (figure 13*c*) and 37.5 (figure 13*d*), a distinct transition from supercritical to subcritical flow is observed near the free surface. Moreover, as D/d increases, corresponding to an

https://doi.org/10.1017/jfm.2026.11716 Published online by Cambridge University Press

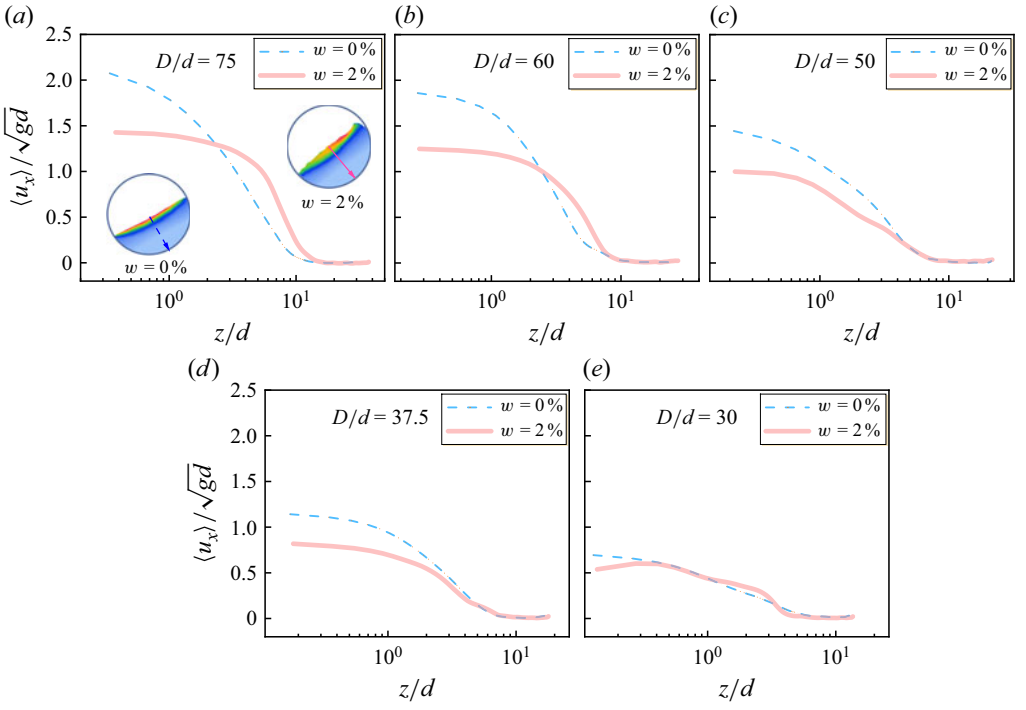


Figure 13. Profiles of the time-averaged particle velocity $\langle u_x \rangle$ normalised by $\sqrt{gd}$ plotted against the normalised depth z/d for dry and cohesive cases with different particle size ratios D/d. Panels show (*a*) $D/d = 75$; (*b*) $D/d = 60$; (*c*) $D/d = 50$; (*d*) $D/d = 37.5$; (*e*) $D/d = 30$. For each case, blue dashed lines correspond to dry granular flows ($w = 0\,\%$), and red solid lines correspond to cohesive flows with $w = 2\,\%$.

enhanced capillary cohesion effect, the velocity profile near the surface becomes nearly flat, indicating that particles begin to flow with the same velocity. This further reflects the transition toward a cohesion-dominated plug flow regime, where the deviation between cohesive and dry cases becomes increasingly pronounced.

Building upon these analyses and observations, figure 14 summarises the evolutions of the normalised flowing layer thickness δ_0/d and the tangent of the dynamic angle of repose $\tan\beta_0$ with the particle size ratio D/d for both dry and cohesive cases. For a given Froude number, a reduction in particle size under identical interstitial fluid properties increases the Bond number, Bo, defined in (2.3) and strengthens capillary cohesion effect, which in turn leads to larger values of both δ_0/d and $\tan\beta_0$. Although no clear functional dependence (e.g. linear or power law) of δ_0/d and $\tan\beta_0$ on D/d is observed for cohesive cases, both quantities remain consistently larger than those in dry cases, indicating that cohesion plays an important role in shaping the macroscopic flow behaviour. Note that the observed changes in the flow dynamics are governed by the combined effects of both size ratio D/d and cohesion. This provides a basis to test whether the proposed dimensionless parameter Q^* can effectively capture these simultaneous influences, as demonstrated in § 3.3.3.

In addition, although the Bond numbers of the cohesive particles are generally below 10 in this study, indicating a weakly cohesive regime, we observed that interparticle cohesion can significantly affect the flow dynamics, as discussed above. Furthermore, regarding the flow regime transition, at lower rotation speeds (e.g.$\omega = 4$ rpm), the addition of 2 % interstitial fluid induces discontinuous avalanches for granular assemblies with $D/d = 60$,

https://doi.org/10.1017/jfm.2026.11716 Published online by Cambridge University Press

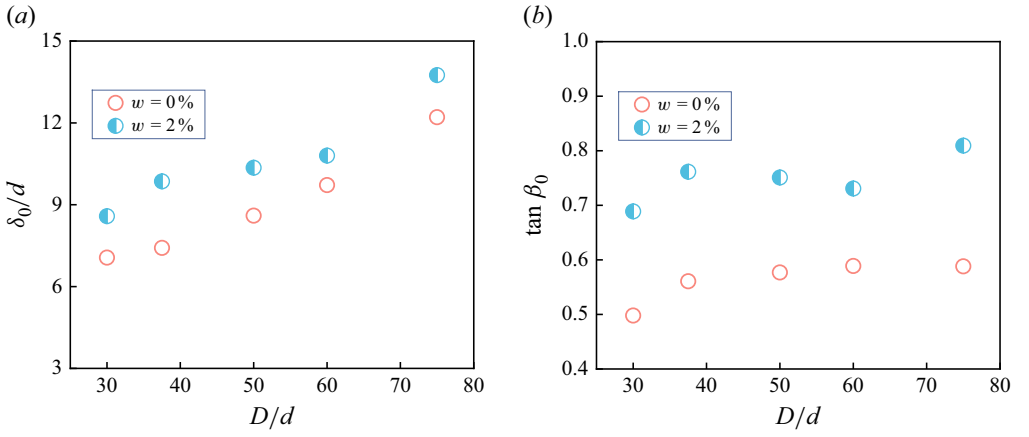


Figure 14. (*a*) Normalised flowing layer thickness δ_0/d and (*b*) tangent of the dynamic angle of repose tan β_0 as functions of the size ratio D/d for both dry and cohesive cases.

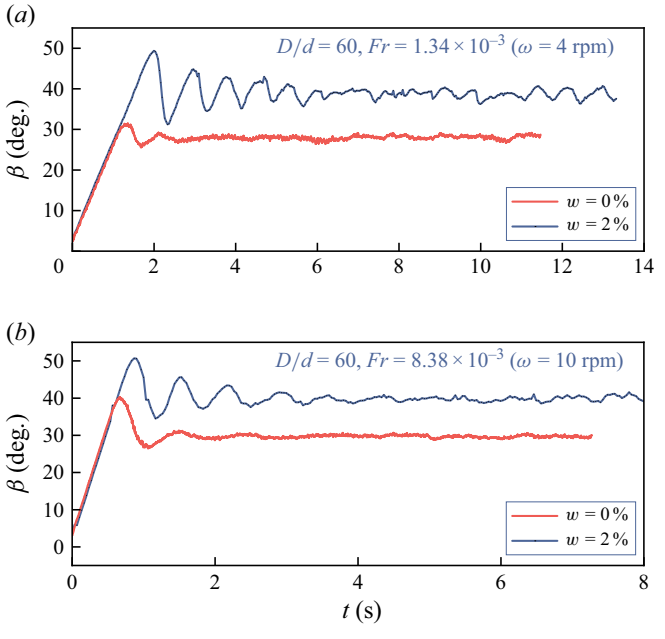


Figure 15. Temporal evolution of the free-surface angle β at $D/d = 60$ for dry and cohesive cases: (*a*) $Fr = 1.34 \times 10^{-3}$; (*b*) $Fr = 8.38 \times 10^{-3}$.

whereas the dry counterpart exhibits continuous flow under the same conditions, as shown in figure 15(*a*). This demonstrates that the cohesion increases the critical rotation speed required to achieve a steady, continuous flow. This study focuses on dense granular flows under relatively weak cohesion and within a rotation speed range that ensures continuous motion, while the intermittent avalanche (slumping) regime is beyond our scope. Therefore, a rotation speed of 10 rpm (figure 15*b*) was selected to ensure that cohesive particles of different sizes achieve continuous flows, which is higher than that required for the cohesionless systems.

https://doi.org/10.1017/jfm.2026.11716 Published online by Cambridge University Press

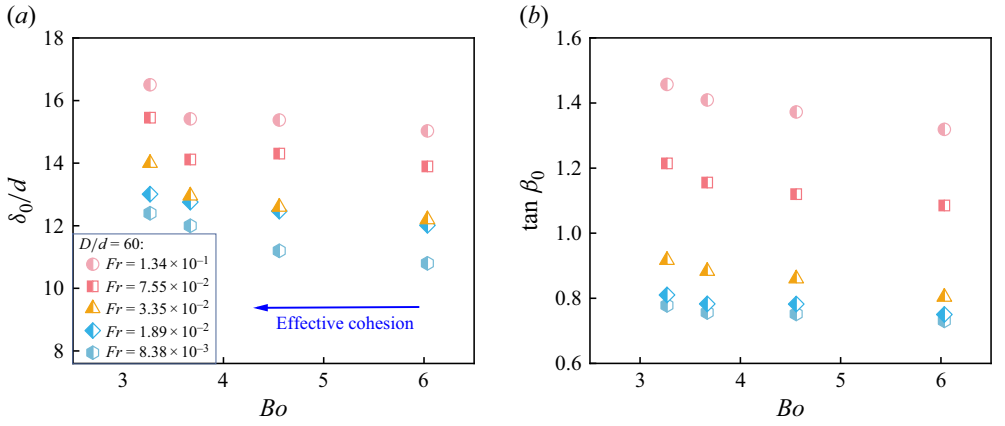


Figure 16. (*a*) Normalised flowing layer thickness δ_0/d and (*b*) tangent of the dynamic angle of repose tan β_0 as functions of the Bond number *Bo* for different Froude numbers *Fr* at a fixed size ratio of $D/d = 60$. The blue arrow indicates that, for cohesive cases with fixed $D/d = 60$, effective cohesion increases with decreasing *Bo*.

3.3.2. *Effect of capillary-induced cohesion*

Particular attention is given to the effects of interstitial fluid properties on the dynamics of cohesive granular flows, since the capillary force between particles in the pendular state partly originates from the surface tension at the liquid–air interface, which directly governs the interparticle cohesion. In this study, the ethanol fraction in the liquid mixtures varies from 0 % (pure water) to 15 % while maintaining a fixed size ratio of $D/d = 60$ and liquid content of $w = 2\,\%$, thereby reducing the *Bo* from 6.03 to 3.27 to achieve different levels of particle cohesion, as listed in table 1.

Figures 16(*a*) and 16(*b*) display the evolution of the normalised flowing layer thickness δ_0/d and the tangent of the dynamic angle of repose tan β_0 as a function of the microscopic Bond number *Bo* defined in (2.3) for different values of Froude numbers *Fr* at a fixed size ratio of $D/d = 60$. Here, $\omega \geq 10$ rpm is used to ensure continuous flows. For a given *Fr*, a systematic decrease in both δ_0/d and tan β_0 is observed with *Bo*. Furthermore, the effect of *Bo* appears to be linked to inertial effects, with tan β_0 showing a more pronounced decline in drums operating at a higher rotation speed, while varying only slightly with *Bo* at lower *Fr*. It should be noted that opposite behaviours have been reported in previous studies, where Preud'homme *et al.* (2021) and Dong *et al.* (2023) observed that particles with a larger *Bo* tend to exhibit a steeper surface slope and a thicker flowing layer. In their simulations, *Bo* was increased by enhancing the surface tension γ at the liquid–air interface while keeping the contact angle θ unchanged, thereby strengthening the capillary cohesion between particles. However, in our experiments, the contact angle inevitably varies with the fluid composition. As listed in table 1, an increase in ethanol mass fraction leads to a systematic reduction in γ, accompanied by a more pronounced increase in cos θ, indicating enhanced wettability of the PMMA surface. Consequently, the effective adhesive term γ cosθ, qualitatively reflecting the effective cohesion (Nase *et al.* 2001; Schaarsberg *et al.* 2016), increases with ethanol concentration despite the decrease in γ alone. In essence, both our results and previous studies reflect the same mechanism, namely that enhanced cohesion promotes a thicker flowing layer and a steeper surface slope.

This phenomenon can be interpreted through a simplified slab-based force balance, similar to that adopted to account for the flow in a confined granular heap (Taberlet *et al.* 2003). Considering a granular slab, parallel to the free surface, with thickness δ_0 and

https://doi.org/10.1017/jfm.2026.11716 Published online by Cambridge University Press

density ρ_p, the downslope driving shear stress acting at the base is

$$\tau\ (\delta_0) = \rho_p g \delta_0 \sin \beta_0. \tag{3.6}$$

The corresponding normal stress at the base of the slab is

$$p\ (\delta_0) = \rho_p g \delta_0 \cos \beta_0. \tag{3.7}$$

Following the Mohr–Coulomb framework, the base of the slab (flowing layer) is treated as a yield surface (Pol *et al.* 2025), with the shear stress τ at the base expressed as

$$\tau = \mu_s p + c, \tag{3.8}$$

where μ_s denotes the effective friction coefficient between the flowing layer and the underlying static granular bed, and c represents the cohesive stress induced by capillary bridges. Equation (3.8) shows that the presence of cohesion increases the resisting shear stress at the base of the flowing layer, thereby requiring a larger driving shear stress to sustain steady flow. Substituting equations (3.6) and (3.7) into (3.8), we obtain

$$\tan \beta_0 = \mu_s + \frac{c}{\rho_p g \delta_0 \cos \beta_0}, \tag{3.9}$$

which clearly clarifies how the system adjusts to increased cohesion. That is, an increase in the cohesive force should be balanced by increasing either the basal normal stress p through a thicker flowing layer, or the downslope driving stress through a steeper surface angle β_0. Under steady flow conditions, both adjustments typically occur concurrently, leading to simultaneous increases in δ_0 and β_0, consistent with the experimentally observed trends in figures 14 and 16.

In addition, for a given cohesion and D/d, both δ_0/d and $\tan \beta_0$ increase systematically with Fr, as presented in figure 16. This behaviour can be rationalised within the same framework. At higher Fr, stronger inertial effects intensify particle collisions and velocity fluctuations, thus generating additional collisional stresses that enhance the total shear resistance. To accommodate this elevated stress and facilitate energy dissipation, the flow develops a thicker layer, allowing more particles to participate in energy dissipation, and a steeper surface that provides greater gravitational driving stress to overcome the enhanced inertial resistance.

3.3.3. *Scaling analysis and unified law*

The results presented in § 3.3 demonstrate that the flow dynamics of cohesive granular materials in a rotating drum is governed by a complex interplay of several dominant parameters, including cohesion, size effects and inertial effects. Among them, cohesion and size effects are strongly coupled and nonlinear, primarily due to the dependence of interparticle capillary forces on particle size, which complicates the establishment of scaling laws for quantitatively describing cohesive granular flows.

Based on the dimensional analysis of cohesive granular flows with the introduction of a capillary time scale, we propose a dimensionless flow rate Q^* for cohesive cases, defined as $Q^* = Fr^{1/2}(D/d)^{3/2}(Bo)^{-1/2}/4$, to quantify the combined effects of cohesion, size and inertial effects, as detailed in § 2.4. Figures 17(a) and 17(b) plot the normalised flowing layer thickness δ_0/d and dynamic angle of repose $\tan \beta_0$, respectively, as functions of the proposed scaling parameter Q^*, covering a wide range of Fr, D/d and Bo values. Both δ_0/d and $\tan \beta_0$ increase with Q^*, reflecting their coupled evolution as discussed in the previous section. Remarkably, all experimental data collapse onto single master curves with respect to Q^*, regardless of the rotation speed, particle size or capillary force. For comparison,

https://doi.org/10.1017/jfm.2026.11716 Published online by Cambridge University Press

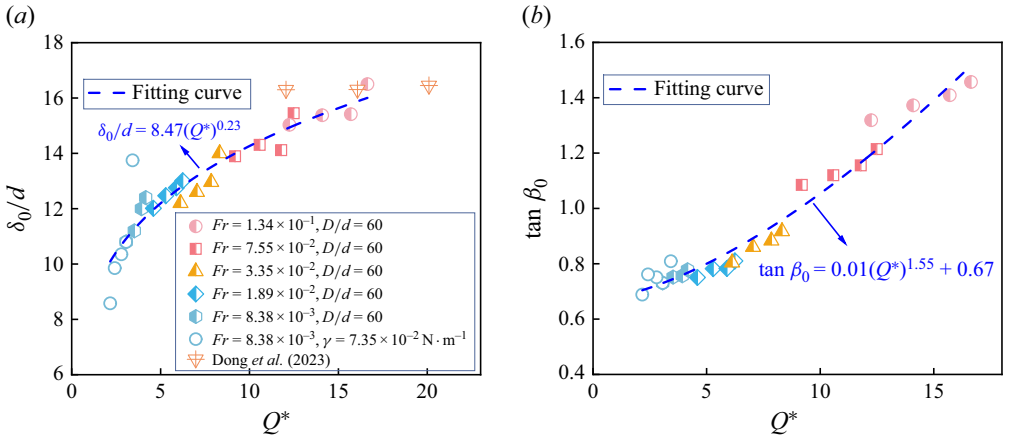


Figure 17. (*a*) Normalised flowing layer thickness δ_0/d and (*b*) tangent of the dynamic angle of repose $\tan\beta_0$ plotted against the proposed scaling parameter Q^* for cohesive cases, covering a wide range of Fr, D/d and Bo values. Open symbols represent cohesive cases with different particle size ratios ($D/d = 30$–75) at fixed surface tension ($\gamma = 7.35\times10^{-2}$ N·m^{-1}) and fixed rotation speed ($Fr = 8.38\times10^{-3}$). Half-filled symbols denote cases with fixed $D/d = 60$, where the capillary strength is varied via the ethanol fraction. Simulation data from Dong *et al.* (2023) are included for comparison ($D/d = 96$, $\gamma = 1.46\times10^{-1}$ N·m^{-1}).

simulation data from Dong *et al.* (2023) are also included and exhibit a similar scaling trend.

Specifically, the datasets in our study follow well-defined power-law relationships, which can be expressed as

$$\delta_0/d = 8.47(Q^*)^{0.23}, \tag{3.10a}$$

$$\tan\beta_0 = 0.01(Q^*)^{1.55} + 0.67. \tag{3.10b}$$

Here, the exponents (0.23 and 1.55) characterise the power-law sensitivity of δ_0/d and $\tan\beta_0$ to the unified parameter Q^*, while the prefactors (8.47 and 0.01) determine the proportionality between these quantities and Q^*. The constant term 0.67 in (3.10*b*) represents an empirical intercept obtained from fitting within our experimental range.

Although the term $\gamma\cos\theta$ plays an important role in qualitatively reflecting the cohesion level at the particle scale, it should be noted that the θ values shown in table 1 correspond to static measurements obtained on a flat PMMA substrate. In the rotating drum, however, the liquid bridges are subject to dynamic deformation and shearing, and the effective contact angle within these dynamic bridges may deviate from the static value. When the measured static θ is explicitly incorporated into a modified Bond number, additional scatter is introduced in the data collapse. It can be observed from figure 17 that the proposed power-law scaling, which employs a conventional Bond number that does not explicitly include θ, remains remarkably effective. This indicates that employing surface tension γ alone provides a consistent basis for establishing a unified scaling law, as γ and θ vary concurrently with liquid composition and are inherently coupled rather than independent control parameters. This approach is consistent with the principle of employing a minimal and physically coherent set of control parameters to capture the underlying physics (Pignatel *et al.* 2012; Man *et al.* 2025).

Overall, these results highlight the robustness and universality of the proposed scaling parameter Q^* in governing the cohesive granular flows by unifying the complex interplay among the key controlling parameters. Furthermore, the proposed scaling law deepens the

https://doi.org/10.1017/jfm.2026.11716 Published online by Cambridge University Press

understanding of the complex flow behaviour of cohesive granular materials. It also has the potential to provide a theoretical foundation for continuum modelling of large-scale geophysical mass movements.

3.4. *Connection to the μ(I) rheology*

Having established the scaling behaviour of δ_0 and β_0 for both dry and cohesive granular materials, it is insightful to interpret these observations within the framework of rheological laws. While more recent frameworks incorporating non-local effects (Kamrin & Koval 2012) or soft-particle interactions (Chialvo, Sun & Sundaresan 2012) have been proposed to capture the complex physics of dense granular flows, their application typically requires spatially resolved internal stress distributions or microscopic contact parameters (e.g. particle stiffness) that cannot be directly measured in the present experiments. Therefore, the classical $\mu(I)$ rheology, linking the friction coefficient μ to a dimensionless shear rate that can be estimated from macroscopic parameters accessible in rotating drums, provides a parsimonious and robust framework for comparing the rheological behaviour of dry and cohesive granular flows, following its recent numerical extensions to cohesive granular systems (Gu, Chialvo & Sundaresan 2014; Mandal *et al.* 2020).

Following a similar approach proposed by Pignatel *et al.* (2012), the friction coefficient μ can be approximated in our experiments by an effective coefficient $\mu_{eff} \approx \tan\beta_0$, which serves as a macroscopic measure of the ratio between shear and normal stresses within the flowing layer under steady states, as also discussed in § 3.3. In addition, the shear rate $\dot{\gamma}$ is made dimensionless to define the inertial number I, which is estimated from the shear rate within the flowing layer, using $I \approx \dot{\gamma} t_d$ for dry and $I \approx \dot{\gamma} t_c$ for cohesive cases, where t_d and t_c are the characteristic inertial and capillary time scales defined in § 2.4. And the shear rate $\dot{\gamma}$ is derived from the flow rate as $\dot{\gamma} \approx (Q/\delta_0)/\delta_0 \approx (1/8)\omega D^2/\delta_0^2$. Within our simplified framework, it is mathematically evident that the inertial number I is not independent but can be expressed as a function of Q^*, given by $I = Q^*/(\delta_0/d)^2$, which is consistent with the results obtained by Pignatel *et al.* (2012). The macroscopic flow structure emerges as a direct consequence of the local rate-dependent rheology.

Figure 18 presents the relationship between the effective friction coefficient μ_{eff} and the inertial number I for both dry and cohesive cases, providing a rheological interpretation of our experimental data based on the above simplifications. A monotonic increase of μ_{eff} with I is observed across nearly all experimental cases, consistent with the general trend predicted by the $\mu(I)$ rheology (Badetti *et al.* 2018; Pouliquen 2025), indicating a rate-dependent strengthening of shear resistance. Compared with the dry cases, the monotonic rheological response of cohesive flows exhibits a higher effective friction coefficient at a given I, capturing the increased flow resistance induced by interparticle capillary cohesion. Given that the cohesion of granular assemblies reflects the enhanced intensity of contact forces, several recent simulations (Abramian, Staron & Lagrée 2020; Vo *et al.* 2020; Deboeuf & Fall 2023) have applied the stress additivity method to extend the applicability of the $\mu(I)$ framework to cohesive systems. Within this framework, the total shear resistance is interpreted as the sum of a frictional term and additional cohesive contributions (Pouliquen 2025). The influence of cohesion can then be incorporated through the definition of a modified inertial number that includes a capillary-like characteristic time scale. Therefore, our experimental findings reveal an enhanced effective friction coefficient in cohesive flows, providing direct evidence for the validity of this stress additivity approach. Furthermore, although strict quantitative comparisons between different studies on cohesive granular flows remain challenging due to variations

https://doi.org/10.1017/jfm.2026.11716 Published online by Cambridge University Press

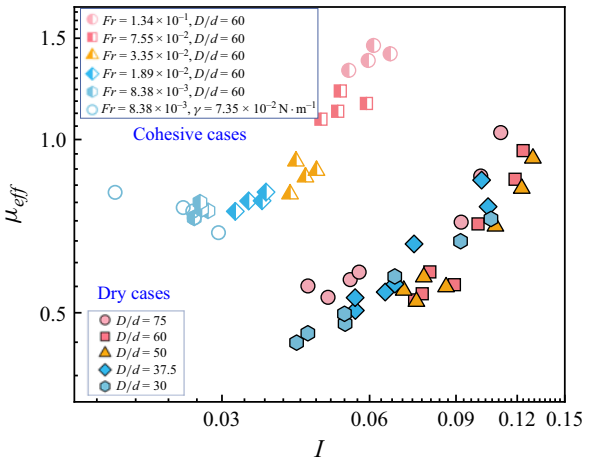


Figure 18. Effective friction coefficient μ_{eff} as a function of inertial number I for all experimental data, covering both dry and cohesive cases.

in particle properties and boundary conditions (Pouliquen 2025), the consistent monotonic increase of μ_{eff} with I across these studies indicates that the underlying physics of cohesive granular flows remains fundamentally governed by a rate-dependent friction law, regardless of the specific flow configuration.

However, small deviations from the $\mu(I)$ rheological trend can be seen in some datasets, which may be attributed to the simplified assumption used in estimating the shear rate. In the present analysis, the shear rate within the flowing layer is treated as a constant, neglecting the spatial variation of the local shear rate and the gradual decay of the streamwise velocity into the bulk, both of which are known to contribute to non-local effects (Liu & Henann 2017). Nevertheless, the current results exhibit a noticeably improved collapse compared with those reported by Pignatel *et al.* (2012), likely due to the reduced effects of wall friction in our experimental set-up, which prevented the complex frictional responses observed in their studies.

Overall, despite the observed small deviations, our experimental results show a good collapse across a wide range of *Fr*, *D/d* and *Bo* values, with the data exhibiting clear rate-dependent frictional behaviour. This demonstrates that the adopted time-scale-based definition of I to a certain extent captures the dominant physics governing both dry and cohesive granular flows.

4. Conclusions

In this work, we have experimentally investigated the steady surface flow of dry and cohesive granular materials in a rotating drum. The effects of rotation speed, drum-to-particle size ratio *D/d* and cohesion strength on flow dynamics, including the velocity field, flowing layer thickness δ_0 and dynamic angle of repose β_0, were examined using PIV and statistical post-processing. In addition, scaling relationships were established to describe both dry and cohesive granular flows by unifying the complex interplay among the key controlling parameters. Our main findings are summarised below.

(i) For dry granular flows, both δ_0/d and $\tan\beta_0$ exhibit a clear positive dependence on the Froude number *Fr*. As *Fr* increases, a transition from the rolling to the cascading regime is observed, while a smaller *D/d* shows a more delayed onset of this transition.

https://doi.org/10.1017/jfm.2026.11716 Published online by Cambridge University Press

A physical interpretation based on a static friction force balance suggests that larger particles experience greater effective Coulombic friction against the sidewalls and stronger lateral confinement, thereby requiring higher rotation speeds to achieve comparable flow dynamics. The dimensionless flow rate Q^* ($Bo \ll 1$) effectively unifies the inertia and size effects, yielding consistent power-law relationships with δ_0/d and $\tan\beta_0$ across different Fr and D/d values. Moreover, a robust correlation between $\tan\beta_0$ and δ_0/d identifies a critical transition angle of $\tan\beta_0 \approx 0.58$, marking the onset of cascading behaviour.

(ii) Compared with cohesionless cases, the presence of interstitial liquid induces capillary bridges that enhance interparticle coupling and internal shear resistance, giving rise to a distinct plug-like regime with a convex free surface, characterised by collective particle motion as quasi-rigid clusters and by larger values of β_0 and δ_0. Smaller particles or higher ethanol contents, through their direct control over the particle-scale cohesive strength, enhance effective cohesion and thereby promote steeper free surfaces and thicker flowing layers. This behaviour is mechanistically explained by a slab-based force-balance model, wherein increased cohesive stress must be compensated by greater basal normal stress through a thicker layer or by enhanced downslope driving stress through a steeper surface. Concurrently, elevated inertia at higher Fr intensifies collisional stresses, further amplifying both δ_0/d and $\tan\beta_0$ to facilitate energy dissipation.

(iii) For cohesive granular materials in a pendular state, a governing dimensionless parameter Q^* was proposed, derived from dimensional analysis incorporating a capillary time scale, to quantify the combined effects of cohesion, size, and inertial effects. Remarkably, nearly all experimental data for δ_0/d and $\tan\beta_0$ collapse onto single master curves when plotted against Q^*, following well-defined power-law relationships across a wide range of Fr, D/d and Bo values. These results highlight the robustness and universality of Q^* as a governing parameter that captures the essential physics of cohesive granular flows.

(iv) A rheological interpretation of our experimental data, linking the effective friction coefficient μ_{eff} to the inertial number I, reveals a monotonic increase of μ_{eff} with I across nearly all experimental cases, consistent with the general trend predicted by the $\mu(I)$ rheology. Compared with the dry cases, the rheological response of cohesive flows exhibits a higher effective friction coefficient at a given I, capturing the increased flow resistance induced by interparticle capillary cohesion. This demonstrates that the adopted definition of I, based on the characteristic time scale, captures to a certain extent the dominant physics governing both dry and cohesive granular flows.

Overall, the proposed scaling law advances the understanding of the dry and cohesive granular flow dynamics and provides a unified framework for modelling large-scale geophysical flows. Despite these advances, the present work remains phenomenological, as it relies primarily on macroscopic observations. Future studies should therefore employ numerical simulations to investigate the micro-mechanical origins of these scaling laws and to validate the proposed framework from a particle-scale perspective, for example, by extracting the non-local $\mu(I)$ rheology to characterise the intrinsic rheological response of the granular system. In addition, the drum length and diameter were kept fixed in the present experiments, which prevents a systematic decoupling of the respective effects of radial (D/d) and axial (W/d) confinement when varying the particle diameter. Although the adopted W/d range lies within the values commonly reported to mitigate sidewall effects (Orpe & Khakhar 2001; Félix *et al.* 2007), the specific particle properties and

https://doi.org/10.1017/jfm.2026.11716 Published online by Cambridge University Press

cohesive conditions considered here may alter the corresponding thresholds. It would also be beneficial for future studies to systematically vary the drum geometry to quantify wall influences and further generalise the proposed scaling framework.

Supplementary movie. Supplementary movie is available at https://doi.org/10.1017/jfm.2026.11716.

Acknowledgements. We thank Professor L. Xie, Dr G. Jin and Ms Q. Chen for inspiring and helpful discussions.

Funding. Funding for this study was received from the Australian Research Council through the Future Fellowship scheme (FT220100515).

Declaration of interests. The authors report no conflict of interest.

Data availability statement. The data supporting this study's findings are openly available from the corresponding author upon reasonable request.

References

Abramian, A., Staron, L. & Lagrée, P.Y. 2020 The slumping of a cohesive granular column: continuum and discrete modeling. *J. Rheol.* **64** (5), 1227–1235.

Alexander, A.W., Chaudhuri, B., Faqih, A., Muzzio, F.J., Davies, C. & Tomassone, M.S. 2006 Avalanching flow of cohesive powders. *Powder Technol.* **164** (1), 13–21.

Artoni, R., Jabaud, B., Pol, A., Richard, P., Le Menn, E. & Tobie, G. 2025 Discrete numerical analysis of cohesive granular flow in a thin rotating drum: flow regimes and cohesion estimation. *Powder Technol.* **480**, 121723.

Badetti, M., Fall, A., Chevoir, F. & Roux, J.N. 2018 Shear strength of wet granular materials: macroscopic cohesion and effective stress: discrete numerical simulations, confronted to experimental measurements. *Eur. Phys. J. E* **41** (5), 68.

Belda, R., Herraez, J.V. & Diez, O. 2005 A study of the refractive index and surface tension synergy of the binary water/ethanol:Influence of concentration. *Phys. Chem. Liq.* **43** (1), 91–101.

Bonamy, D., Daviaud, F. & Laurent, L. 2002 Experimental study of granular surface flows via a fast camera: a continuous description. *Phys. Fluids* **14** (5), 1666–1673.

Bouchut, F., Fernández-Nieto, E.D., Mangeney, A. & Narbona-Reina, G. 2016 A two-phase two-layer model for fluidized granular flows with dilatancy effects. *J. Fluid Mech.* **801**, 166–221.

Brewster, R., Grest, G.S. & Levine, A.J. 2009 Effects of cohesion on the surface angle and velocity profiles of granular material in a rotating drum. *Phys. Rev. E* **79** (1), 011305–011305.

Castellanos, A., Valverde, J.M., Pérez, A.T., Ramos, A. & Watson, P.K. 1999 Flow regimes in fine cohesive powders. *Phys. Rev. Lett.* **82** (6), 1156.

Chen, Y., Suo, S., Dong, M., Zhong, H., Wei, D. & Gan, Y. 2024 Effects of particle density and fluid properties on mono-dispersed granular flows in a rotating drum. *Phys. Fluids* **36** (10), 103324.

Chialvo, S., Sun, J. & Sundaresan, S. 2012 Bridging the rheology of granular flows in three regimes. *Phys. Rev. E* **85** (2), 021305.

Chou, S.H. & Hsiau, S.S. 2012 Dynamic properties of immersed granular matter in different flow regimes in a rotating drum. *Powder Technol.* **226**, 99–106.

Coppin, N., Henry, M., Cabrera, M., Azéma, E., Dubois, F., Legat, V. & Lambrechts, J. 2023 Collapse dynamics of two-dimensional dry and immersed granular columns of elongated grains. *Phys. Rev. Fluids* **8** (9), 094303–094303.

Courrech du Pont, S., Gondret, P., Perrin, B. & Rabaud, M. 2003 Granular avalanches in fluids. *Phys. Rev. Lett.* **90** (4), 044301–044301.

Dai, G., Zhang, A., Hu, Y., Mao, W., Huang, Y., Hua, Y., Yang, H., Zhang, J. & Zheng, H. 2025 The granular dynamic and flow regime transition of wet granular materials. *J. Fluid Mech.* **1022**, A26–A26.

Deboeuf, S. & Fall, A. 2023 Cohesion and aggregates in unsaturated wet granular flows down a rough incline. *J. Rheol.* **67** (4), 909–909.

Dong, M., Wang, Z., Marks, B., Chen, Y. & Gan, Y. 2023 Partially saturated granular flow in a rotating drum: the role of cohesion. *Phys. Fluids* **35** (11), 113302.

Félix, G., Falk, V. & D'Ortona, U. 2007 Granular flows in a rotating drum: the scaling law between velocity and thickness of the flow. *Eur. Phys. J. E* **22** (1), 25–31.

MiDi, G.D.R. 2004 On dense granular flows. *Eur. Phys. J. E* **14** (4), 341–365.

https://doi.org/10.1017/jfm.2026.11716 Published online by Cambridge University Press

GEE, M.J.R., UY, H.S., WARREN, J., MORLEY, C.K. & LAMBIASE, J.J. 2007 The Brunei slide: a giant submarine landslide on the North West Borneo Margin revealed by 3D seismic data. *Mar. Geol.* **246** (1), 9–23.

GOVENDER, I. 2016 Granular flows in rotating drums: a rheological perspective. *Miner. Engng* **92**, 168–175.

GU, Y., CHIALVO, S. & SUNDARESAN, S. 2014 Rheology of cohesive granular materials across multiple dense-flow regimes. *Phys. Rev. E* **90** (3), 032206–032206.

HALSEY, T.C. & LEVINE, A.J. 1998 How sandcastles fall. *Phys. Rev. Lett.* **80** (14), 3141–3144.

HILL, K.M., GIOIA, G. & TOTA, V.V. 2003 Structure and kinematics in dense free-surface granular flow. *Phys. Rev. Lett.* **91** (6), 064302.

JAIN, N., OTTINO, J.M. & LUEPTOW, R.M. 2005 Regimes of segregation and mixing in combined size and density granular systems: an experimental study. *Granul. Matt.* **7** (2–3), 69–81.

JARRAY, A., MAGNANIMO, V. & LUDING, S. 2019 Wet granular flow control through liquid induced cohesion. *Powder Technol.* **341**, 126–139.

JIN, G., ZHOU, Z., LIU, Y., GAO, C., XIE, Y. & TAO, G. 2025 A coarse-grained discrete element method based on the principle of energy density mapping conservation: efficient simulation of particle dynamic mixing and interaction using larger particles. *Phys. Fluids* **37** (1), 013377.

KAMRIN, K. & KOVAL, G. 2012 Nonlocal constitutive relation for steady granular flow. *Phys. Rev. Lett.* **108** (17), 178301.

KHAMSEH, S., ROUX, J.-N. & CHEVOIR, F. 2015 Flow of wet granular materials: a numerical study. *Phys. Rev. E* **92** (2), 022201.

KHATTAB, I.S., BANDARKAR, F., FAKHREE, M.A.A. & JOUYBAN, A. 2012 Density, viscosity, and surface tension of water+ethanol mixtures from 293 to 323K. *Korean J. Chem. Engng* **29** (6), 812–817.

KIM, S. & KAMRIN, K. 2020 Power-law scaling in granular rheology across flow geometries. *Phys. Rev. Lett.* **125** (8), 088002.

LARIJANI, R.S., MAGNANIMO, V. & LUDING, S. 2025 A Coarse-Grained Discrete Element Model (CG-DEM) based on parameter scaling for dense wet granular system. *Powder Technol.* **453**, 120581.

LI, L. & ANDRADE, J.E. 2020 Identifying spatial transitions in heterogenous granular flow. *Granul. Matt.* **22** (2), 52–52.

LI, P., WANG, D. & NIU, Z. 2022 Unchannelized collapse of wet granular columns in the pendular state: dynamics and morphology scaling. *Phys. Rev. Fluids* **7** (8), 084302–084302.

LIAO, C.-C. & HUANG, Y.-Y. 2021 Experimental investigate the effect of liquid distribution state on size segregation of wet granular materials in rotating drums. *Powder Technol.* **381**, 561–566.

LIU, D. & HENANN, D.L. 2017 Non-local continuum modelling of steady, dense granular heap flows. *J. Fluid Mech.* **831**, 212–227.

LIU, P.Y., YANG, R.Y. & YU, A.B. 2011 Dynamics of wet particles in rotating drums: effect of liquid surface tension. *Phys. Fluids* **23** (1), 013304.

LIU, X., ZHOU, A., SHEN, S.-L., LI, J. & ARULRAJAH, A. 2021 Modelling unsaturated soil-structure interfacial behavior by using DEM. *Comput. Geotech.* **137**, 104305–104305.

LUCAS, A., MANGENEY, A. & AMPUERO, J.P. 2014 Frictional velocity-weakening in landslides on Earth and on other planetary bodies. *Nat. Commun.* **5** (1), 3417–3417.

MA, H. & ZHAO, Y. 2018 Investigating the flow of rod-like particles in a horizontal rotating drum using DEM simulation. *Granul. Matt.* **20** (3), 41–41.

MAGUIRE, E.S.F., BARKER, T., RAUTER, M., JOHNSON, C.G. & GRAY, J.M.N.T. 2024 Particle-size segregation patterns in a partially filled triangular rotating drum. *J. Fluid Mech.* **979**, A40.

MAN, T., HUPPERT, H.E. & GALINDO-TORRES, S.A. 2025 Run-out scaling of granular column collapses on inclined planes. *J. Fluid Mech.* **1002**, A50–A50.

MAN, T., HUPPERT, H.E., LI, L. & GALINDO-TORRES, S.A. 2021 Finite-size analysis of the collapse of dry granular columns. *Geophys. Res. Lett.* **48** (24), e2021GL096054.

MAN, T., WANG, Z., HUPPERT, H., REN, S., GALINDO-TORRES, S.A., ZHANG, X. & ZHOU, A. 2026 Propagation scaling and micromechanics of buoyant granular column collapses. *J. Geophys. Res.: Earth Surf.* **131** (3), e2025JF008812.

MANDAL, S., NICOLAS, M. & POULIQUEN, O. 2020 Insights into the rheology of cohesive granular media. *Proc. Natl Acad Sci. USA* **117** (15), 8366–8373.

MARI, S.S. & RAJU, G. 2021 A new framework for contour tracing using Euclidean distance mapping. *Intl J. Comput. Vis. Robot.* **11** (5), 542.

MARTEAU, E. & ANDRADE, J.E. 2018 A model for decoding the life cycle of granular avalanches in a rotating drum. *Acta Geotech.* **13** (3), 549–555.

MELLMANN, J. 2001 The transverse motion of solids in rotating cylinders—forms of motion and transition behavior. *Powder Technol.* **118** (3), 251–270.

https://doi.org/10.1017/jfm.2026.11716 Published online by Cambridge University Press

NASE, S.T., VARGAS, W.L., ABATAN, A.A. & MCCARTHY, J.J. 2001 Discrete characterization tools for cohesive granular material. *Powder Technol.* **116** (2-3), 214–223.
NEVEU, A., FRANCQUI, F. & LUMAY, G. 2022 Measuring powder flow properties in a rotating drum. *Measurement* **200**, 111548.
NIU, W., ZHENG, H., YUAN, C., MAO, W. & HUANG, Y. 2024 Shear characteristics of granular materials with different friction coefficients based on ring shear test. *Granul. Matt.* **26** (2), 26–26.
NOWAK, S., SAMADANI, A. & KUDROLLI, A. 2005 Maximum angle of stability of a wet granular pile. *Nat. Phys.* **1** (1), 50–52.
OBA, H. & OTSUKI, M. 2026 Scaling laws for velocity profile of granular flow in rotating drums. *Phys. Fluids* **38** (2), 023312.
OROZCO, L.F., DELENNE, J.-Y., SORNAY, P. & RADJAI, F. 2020 Rheology and scaling behavior of cascading granular flows in rotating drums. *J. Rheol.* **64** (4), 915–931.
ORPE, A.V. & KHAKHAR, D.V. 2001 Scaling relations for granular flow in quasi-two-dimensional rotating cylinders. *Phys. Rev. E* **64** (3), 031302–031302.
ORPE, A.V. & KHAKHAR, D.V. 2007 Rheology of surface granular flows. *J. Fluid Mech.* **571**, 1–32.
OTTINO, J.M. & KHAKHAR, D.V. 2000 Mixing and segregation of granular materials. *Annu. Rev. Fluid Mech.* **32** (1), 55–91.
PIGNATEL, F., ASSELIN, C., KRIEGER, L., CHRISTOV, I.C., OTTINO, J.M. & LUEPTOW, R.M. 2012 Parameters and scalings for dry and immersed granular flowing layers in rotating tumblers. *Phys. Rev. E* **86** (1), 011304–011304.
POL, A., ARTONI, R. & RICHARD, P. 2025 Cohesive granular material in a rotating drum: flow regimes and size effects. *J. Fluid Mech.* **1006**, A24.
POULIQUEN, O. 2025 Powders and cohesive granular media: a rheological perspective. *Rheol. Acta* **64** (4), 195–207.
PREUD'HOMME, N., LUMAY, G., VANDEWALLE, N. & OPSOMER, E. 2021 Numerical measurement of flow fluctuations to quantify cohesion in granular materials. *Phys. Rev. E* **104** (6), 064901–064901.
RAJCHENBACH, J. 1990 Flow in powders: from discrete avalanches to continuous regime. *Phys. Rev. Lett.* **65** (18), 2221–2224.
ROGNON, P.G., ROUX, J.-N., NAAÏM, M. & CHEVOIR, F. 2008 Dense flows of cohesive granular materials. *J. Fluid Mech.* **596**, 21–47.
ROY, S., LUDING, S. & WEINHART, T. 2017 A general (ized) local rheology for wet granular materials. *New J. Phys.* **19** (4), 043014.
SANVITALE, N., ZHAO, B.D., BOWMAN, E.T. & O'SULLIVAN, C. 2023 Particle-scale observation of seepage flow in granular soils using PIV and CFD. *Géotechnique* **73** (1), 71–88.
SCHAARSBERG, M.H.K., PETERS, I.R., STERN, M., DODGE, K., ZHANG, W.W. & JAEGER, H.M. 2016 From splashing to bouncing: the influence of viscosity on the impact of suspension droplets on a solid surface. *Phys. Rev. E* **93** (6), 062609–062609.
TABERLET, N., RICHARD, P., VALANCE, A., LOSERT, W., PASINI, J.M., JENKINS, J.T. & DELANNAY, R. 2003 Superstable granular heap in a thin channel. *Phys. Rev. Lett.* **91** (26), 264301–264301.
TEGZES, P., VICSEK, T. & SCHIFFER, P. 2003 Development of correlations in the dynamics of wet granular avalanches. *Phys. Rev. E* **67** (5), 051303–051303.
THIELICKE, W. & SONNTAG, R. 2021 Particle Image Velocimetry for MATLAB: accuracy and enhanced algorithms in PIVlab. *J. Open Res. Softw.* **9** (1), 12–12.
THIELICKE, W. & STAMHUIS, E.J. 2014 PIVlab – towards user-friendly, affordable and accurate digital particle image velocimetry in MATLAB. *J. Open Res. Softw.* **2**, e30.
THOMPSON, E.L. & HUPPERT, H.E. 2007 Granular column collapses: further experimental results. *J. Fluid Mech.* **575**, 177–186.
VO, T.T., NEZAMABADI, S., MUTABARUKA, P., DELENNE, J.-Y. & RADJAI, F. 2020 Additive rheology of complex granular flows. *Nat. Commun.* **11** (1), 1476–1476.
VU, D.C., AMARSID, L., DELENNE, J.Y., RICHEFEU, V. & RADJAI, F. 2024 Rheology and scaling behavior of polyhedral particle flows in rotating drums. *Powder Technol.* **434**, 119338.
WANG, W., BARÉS, J., RENOUF, M. & AZÉMA, E. 2025 Flow regimes and repose angle in a rotating drum filled with highly concave particles. *Phys. Rev. E* **112** (1), 015417.
WANG, Z., GUO, W., DING, W., LIU, K., QIN, W., WANG, C. & WANG, Z. 2023 Numerical study on the hydrodynamic properties of bentonite slurries with Herschel-Bulkley-Papanastasiou rheology model. *Powder Technol.* **419**, 118375–118375.
WANG, Z., ZHOU, A., MAN, T. & HUPPERT, H.E. 2026*a* Modelling density segregation in immersed binary granular column collapse through the coupled LBM-DEM method. *Comput. Geotech.* **191**, 107785.

https://doi.org/10.1017/jfm.2026.11716 Published online by Cambridge University Press

WANG, Z., ZHOU, A., MAN, T., XIE, L. & HUPPERT, H.E. 2026*b* Collapse dynamics of immersed granular columns with various particle–fluid density ratios: insights from LBM-DEM coupled modelling. *Acta Geotech.* **21** (1), 371–394.

YANG, G.C., JING, L., KWOK, C.Y. & SOBRAL, Y.D. 2020 Pore-scale simulation of immersed granular collapse: implications to submarine landslides. *J. Geophys. Res.: Earth Surf.* **125** (1), e2019JF005044.

YANG, R.Y., YU, A.B., MCELROY, L. & BAO, J. 2008 Numerical simulation of particle dynamics in different flow regimes in a rotating drum. *Powder Technol.* **188** (2), 170–177.

ZHANG, X., HUANG, T., GE, Z., MAN, T. & HUPPERT, H.E. 2025 Infiltration characteristics of slurries in porous media based on the coupled Lattice-Boltzmann discrete element method. *Comput. Geotech.* **177**, 106865.

ZHAO, C.-F., KRUYT, N.P. & MILLET, O. 2020 Capillary bridges between spherical particles under suction control: rupture distances and capillary forces. *Powder Technol.* **360**, 622–634.

ZHAO, H., AN, X., GOU, D., ZHAO, B. & YANG, R. 2018 Attenuation of pressure dips underneath piles of spherocylinders. *Soft Matt.* **14** (21), 4404–4410.

https://doi.org/10.1017/jfm.2026.11716 Published online by Cambridge University Press